Swiss Society for
Biomedical Engineering

zh
aw
School of
Engineering
IMES Institute of
Mechanical Systems

Annual Meeting of the Swiss Society for Biomedical Engineering SSBE

Winterthur, Sept. 5th 2024

Abstract book

Anton Paar
DELSYS EUROPE
LIMESS Messtechnik & Software GmbH
odne transforming endo
RMS
SHL MEDICAL
schulthess klinik
TEMECO Services TESTEN MESSEN CONSULTING
Zwick Roell
prins Patent-, Marken- & Rechtsanwälte
KISTLER measure. analyze. innovate.
KLINIKEN VALENS
satw it's all about technology

Welcome address

Dear Colleagues & Friends,

It is a pleasure to welcome you to the 2024 Annual Meeting of the Swiss Society of Biomedical Engineering SSBE in Winterthur. The one-day symposium aims to present recent scientific findings and will discuss current innovations aiming to support clinical and surgical developments.

During the conference, we will have the following highlights:

- Keynote lectures of PD Dr. Prabitha Urwyler, Innosuisse, and Prof. Dr. Jörg Mayer, Surgical Fusion Technologies
- Eight oral contributions divided in two scientific sessions which were selected out of more than 40 submitted abstracts
- The award session with three presenting nominees for the SSBE research award and the student award winner's presentation

The meeting will cover a broad range of topics in biomedical engineering, ranging from basic research to clinical applications. An exciting exchange at the poster session is expected which will take place during lunch time and coffee breaks.

We are looking forward to the exchange among the SSBE community which will contribute to the diagnosis and treatment of patients and finally to an improved clinical outcome. The triangle: Clinics – MedTech industry – University may therefore provide a substantial impact.

The organizing committee of the IMES Institute of Mechanical Systems as part of the ZHAW is proud to hold the SSBE conference 2024 in the year of celebrating 150 years "Technikum Winterthur" and 25 years Biomechanical Engineering BME.

Daniel Baumgartner

D. B

In the name of the SSBE organization team

SSBE Board Member "Industry Relations"

1 Venue

Zurich University of Applied Sciences ZHAW
Technikumstrasse 71
Room TN E0.54 (Ground floor)
8401 Winterthur

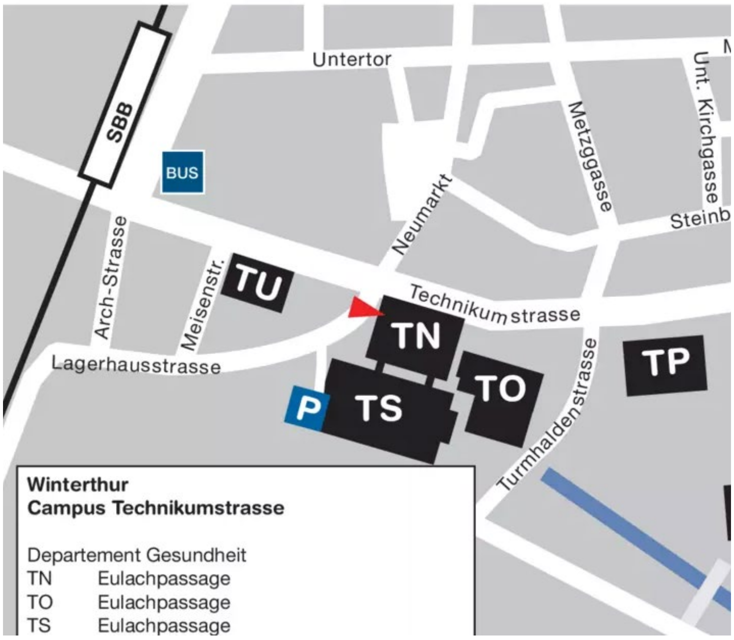

The distance from the train station Winterthur to the conference site in the TN-building is approximately 300m or 10 min walking time.

2 Program, Sept. 5th 2024

09:15 Welcome coffee, registration, placing posters

09:30 Welcome address by SSBE President Bert Müller

09:35 Keynote lecture: PD Dr. Prabitha Urwyler, Innosuisse
"Exploring Unconventional Career Paths & Unlocking Innovation with Innosuisse"

10:15 Coffee break & Poster session

11:00 Oral Session I: presentations of SSBE Members

12:00 Lunch

13:00 SSBE General assembly

14:00 Keynote Lecture: Prof. Dr. Jörg Mayer, Surgical Fusion Technologies
"SupraFusion - insights into a novel, minimally invasive technology for soft tissue to bone fixation"

14:30 Oral Session II: presentations of SSBE Members

15.30 Refreshments at the posters

16:00 Award session for the SSBE Research Award:

1 Johanna Franziska Menze, University of Berne, "Towards subject-specificity in biomechanical modelling of rotator cuff pathologies and interventions"

2 Thijs Smit, ETH Zurich, "Topology optimization of patient-specific spinal fusion implants"

3 Theofanis Stampoultzis EPFL, "Enhancing Chondrocyte Biosynthetic Activities: Harnessing the Power of Loading-Induced Evolved Temperature"

Winner of the SSBE Student Award:

L. Constantin - PPG-based sleep staging using sleepPPGNet: extension to wearables, improvements

17:00 25 Years Biomechanical Engineering & 150 Years "Technikum Winterthur"

Accompanied by life music from Jonas & Philipp

17:25 Award Session of the SSBE Research Award

17:30 Closing remarks & Opening of the Dinner

3 Keynotes

3.1 Keynote lecture I: PD Dr. Prabitha Urwyler, Innosuisse (09.35 am)

Exploring Unconventional Career Paths & Unlocking Innovation with Innosuisse

Abstract

In an era where traditional career trajectories are increasingly being redefined, exploring unconventional career paths has become essential for personal and professional growth. In the first part of this presentation, I will share my personal journey navigating non-linear career paths within the Swiss landscape, highlighting the importance of adaptability, networking, and continuous learning in shaping a dynamic and successful career.

The second part of the presentation will focus on the pivotal role of Innosuisse—Switzerland's Innovation Agency—in promoting innovation. Attendees will gain insights into the various programs and opportunities offered by Innosuisse that empower entrepreneurs, researchers, and industry leaders to transform their innovative ideas into successful ventures

CV Prabitha Urwyler

Prabitha Urwyler is the Scientific Officer and Program Manager for Bilateral Cooperation at Innosuisse, the Swiss Innovation Agency, a role she has held since July 2021. With a unique blend of experience spanning over software engineering within the tech and media sectors, and an accomplished career in clinical research, Prabitha brings a wealth of interdisciplinary expertise to her current position.

Her academic credentials include a Bachelor of Technology in Computer Science & Engineering from Mangalore University (1995), an M.Sc. in Biomedical Engineering from the University of Bern (2008), a Ph.D. in Biomedical Engineering from the University of Basel and the Paul Scherrer Institute (2012), and a Venia Docenti (PD, habilitation) from the University of Bern (2019).

Prabitha's research career is marked by significant contributions in fields such as nanotechnology, biosensors, biomaterials, implant surfaces, neuroscience, psychiatry, and gerontechnology. She has held prominent roles including Deputy Group Leader at the Gerontechnology and Rehabilitation Group at the ARTORG Center of the University of Bern.

Beyond her professional achievements, Prabitha is deeply committed to gender equality and community engagement. She has served as the Gender Equality Officer of the ARTORG Center and was the founding president of the Biomedical Engineering Club Bern. Additionally, she holds leadership roles in various organizations, including the Swiss Chess Federation and the FIDE social commission.

Prabitha Urwyler's diverse and impactful career makes her a dynamic leader in both the scientific and diplomatic communities, driving innovation and fostering collaboration across disciplines.

3.2 Keynote lecture II: PhD Jörg Mayer, Surgical Fusion Technologies GmbH (2 pm)

SupraFusion® - Insights into a Novel, Minimally Invasive Technology for Soft Tissue to Bone Fixation

Abstract

Repair of structural soft tissues like ligaments and tendons faces some clinical challenges. Besides the poor vascularization and regeneration capacity of the ligaments and tendons, optimal fixation is achieved by placing suture anchors as anatomically as possible. This means fixation primarily in cancellous bone, an area with limited accessibility and bone quality. For early rehabilitation, though, the joint should be remobilized quickly, thus exposing the anchor to significant fatigue and creep loading. The SupraFusion® Technology provides a new approach to the above-mentioned clinical challenge. Instead of using mechanical fixation by threads or barbs or similar, the anchor is implanted with the aid of ultrasonic vibrations that lead to liquefaction of the anchor's polymeric surface. The liquefied portion of the polymer infiltrates and augments the adjacent cancellous bone structure. The lecture will provide an insight into the underlying basics of the SupraFusion® Technology and the impact of ultrasonic liquefaction on biocompatibility and biomechanical behavior. Based on the current, clinically used suture anchors, the potential of the technology for providing minimally invasive solutions to Sports Medicine will be discussed.

CV Jörg Mayer

Dr. Joerg Mayer graduated from ETH Zurich with a master's in Material Science and received his Ph.D. for his research on a new generation of composite materials for orthopedic applications. For 13 years, together with Prof. Dr. E. Wintermantel, he was co-leading the Chair of Biocompatible Material Science and Engineering at the ETH focusing on anisotropic materials and their processing for orthopedics, wound regeneration, and tissue engineering applications. During this time, four start-up companies were built, and in 2001, together with a cross-disciplinary team, he initiated the LifeScience Park Zurich which led to today's BioTechnopark® Schlieren-Zürich with more than 50 companies and 1500 working places in Life Science and MedTech, and a deal flow of multi-billion CHF over the last 20 years. In 2002, he joined WoodWelding SA as group CTO to build their ultrasonic fixation technology and develop it for orthopedic applications through licensing and spin-out companies in Spine, Veterinary Orthopedics, Ultrasonic Osteotomy, and Sports Medicine. The latter is Joerg's today's focus at Surgical Fusion Technologies GmbH, developing an implant portfolio for soft tissue to bone fixation that is currently introduced in the US market.

For his research and development work, he received several awards, e.g. the Silver Medal of the ETH Zurich, the ETH – T.I.T. Award, the first Swiss Medtech Award in 2005, Swiss Economy Award in 2006, and the Spine Technology Award in 2009. He co-authored more than 300 publications and presentations, more than 90 patents, and several FDA and CE approvals. He is sharing his knowledge by lecturing at the ETH Zurich.

4 Oral Presentations

4.1 Oral Session I: 11.00 am

1	Daniel Carroll - Developing a new robot based testing methodology to deepen clinical investigations surrounding the knee joint	p.10
2	Adela Weil - In-vitro dental implant primary stability: staircase predicting continuous method	p.11
3	Elisa R. Rosanò - Impact of spinal sagittal alignment and body shape on spine biomechanics in adult spinal deformity	p.12
4	Linus Taenzer - Viscoelastic material identification based on experimental data using model order reduction	p.13

4.2 Oral Session II: 2.30 pm

5	Janine Schulte - Evaluation of a new collection technique for touch DNA: the DNA-Buster	p.14
6	Lena Sauerzopf - Transforming clinical assessments: rater reliability in video-based evaluation of upper extremity after stroke	p.15
7	Osman Berk Satir - µCT images from clinical CT of the human proximal femur using deep learning	p.16
8	Johannes Niermann - Bone conduction hearing: methods for the validation of computational models	p.17

5 Poster session

The poster sessions with presence of the author(s) are from 10.15 – 11.00 am. and 3.30 – 4.00 pm. The room is accessible the whole day for visits.

5.1 Imaging & Image Analysis

9	Marta Girona Alarcón - Intravital imaging of the mouse central nervous system	p.18
10	Mattia Humbel - A tomography slice through the entire human brain with less than three micrometer voxels	p.19
11	Marco Mathys - Automating ground truth mask generation for low-contrast CT phantom scans	p.20
12	Daphne Schönegg - Micron-resolution imaging of palatal anatomy with computed tomography	p.21
13	Patrik Wili - Photon-counting CT: a comparative study for bone volume fraction measurement	p.22
14	Cristina Sainz Martinez - Simultaneous electroencephalography and functional magnetic resonance imaging at 7 Tesla: human evaluation	p.23

5.2 Signal processing

15	Foskien Bouman - Benefits of piezoelectric measurement technology in biomechanics and life science	p.24
16	Loïc Jeanningros - Abnormal cardiac rhythm detection from photoplethysmography signals	p.25
17	Omar Lone - Python-based open software for EEG-based brain-machine interfaces	p.26
18	C. Mendez Schneider - Associations between nocturnal hypoglycaemia and consumer-grade sensor data in people with diabetes	p.27
19	Payam S. Shabestari - Advances on real time M/EEG neural feature extraction	p.28
20	Céline Vergne - Towards a robust electromagnetic tracking system for deep brain stimulation surgery	p.29

5.3 Biomechanical Engineering

21	Basil Achermann - Velocity based training: prediction of maximal strength	p.30
22	Philippe Bähler - Musculoskeletal modeling of the scoliotic spine: sensitivity of joint center positions	p.31
23	Andrea Kilchenmann - Preliminary study on measuring balance and control in the elderly using AR and VR technologies	p.32
24	Marwen Mokni - Holoreach: VR trunk control therapy - towards a user friendly experience	p.33
25	Martin E. Birchmeier - Statistical shape modelling in shoulder MRI – an approach to identifying risks for rotator cuff tear pathology	p.34
26	Eva Herbst - Testing scapulothoracic ellipsoid joint implementations using kinematics from biplanar fluoroscopy	p.35
27	Pezhman Eghbali - Estimation of the preoperative variables effect on postoperative total shoulder arthroplasty complications	p.36

5.4 Biomaterials science & engineering

5.5 Swiss medtech

We would like to thank our sponsors for the support of the SSBE 2024 Conference in Winterthur!

Personal Notes:

DEVELOPING A NEW ROBOT BASED TESTING METHODOLOGY TO DEEPEN CLINICAL INVESTIGATIONS SURROUNDING THE KNEE JOINT

Daniel Carroll* (1), Jonas Hofmann (1), Jean-Romain Delaloye (2), Michaela Nusser (1)

1. *Zurich University of Applied Science, School of Engineering, Switzerland*
2. *Clinic of Orthopaedics and Traumatology, Department of Surgery, Kantonsspital, Winterthur, Switzerland*

*Corresponding author: caor@zhaw.ch

Introduction

Industrial robots have become widely used for studying human joint kinematics, particularly in the context of knee motion research. Previous research focused mainly on quasi-static loading, but recent trials have shifted the focus to dynamic tests mimicking *in-vivo* motion, enhancing the investigation of joint biomechanics [1-4]. This study aims to develop a physiologically relevant robotic test to simulate human walking on cadaveric knees accounting for the inherent variation in knee geometries through specimen specific gait adaption. Although similar tests have been conducted [5], this study evaluates the tests impact and utility through comparison with conventional laxity tests.

Material and Methods

The six degree of freedom movement of the knee joint during normal walking has been previously studied. The resultant trajectory will serve as a reference positional input for the robotic walking gait [6].

Firstly, a standard walk will apply the baseline gait trajectory to an ACL deficient knee, adjusted based on a force-corrected starting point. Perturbations from meniscus surgeries A, B and C will be introduced, and results compared to a laxity test for comparison.

Secondly, an adaptive trajectory will dynamically adjust the standard walk to ensure that the resulting force and torque in the proximal/distal and varus/valgus directions align with values reported in the literature [7].

In each case, the knee will undergo ten cycles of the path (standard or adaptive), with average values from the final three cycles used for analysis.

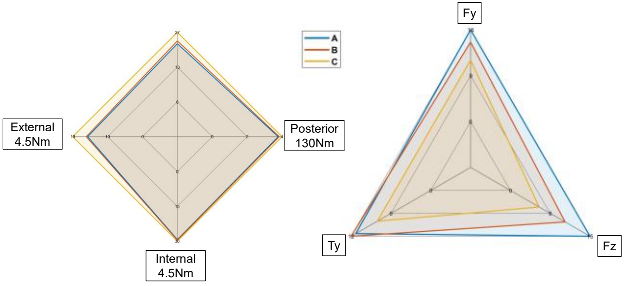

Figure 1: Laxity results for 60° flexion (left) and walking gait results at mid stance (right).

Results

Laxity tests show anterior shifts of 22-23 mm at 60° for states A and B, and 26.5 mm for state C. External rotations at the same angle are -15.29° for A, -15.69° for B, and -20.42° for C, with minimal differences in other laxity tests. At mid-stance for the standard walk, state A generates the highest forces and torques (5N, 18N and 11Nm in the proximal, posterior and valgus directions respectively), while state C generates the lowest (5.5N, 12N and 7.9Nm). Results are detailed in Figure 1. Figure 2 demonstrates the measured force and torque outputs for proximal/distal and varus/valgus respectively, for both the standard and adapted walk.

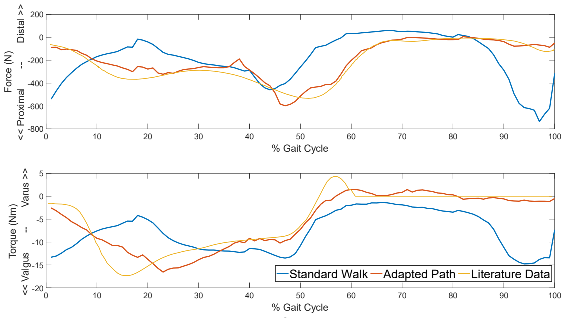

Figure 2: Proximal/distal force (top) and varus/valgus torque (bottom) for standard and adapted path.

Discussion

Lower forces and torques for the state C standard walk correspond to greater laxity, a logical result since lower forces produce less resistance to movement. The reverse is true for state A. While the laxity tests suggest state B is marginally more lax than state A, the difference is more apparent in the walk test, suggesting enhanced discriminative power. However, a larger test set will be required for confirmation, and the knee ACL deficiency, due its use in a prior study, likely influenced the results. The standard walk produced force/torque outputs which deviated from the literature data, likely due in part to specimen specific geometry characteristics. The adapted path produced outputs more closely aligning to the literature, highlighting the potential for robotic automation to produce an individualised, physiologically relevant walking gait.

Acknowledgement

We thank Innosuisse – Swiss Agency for Innovation – for supporting this work.

References

[1] Bates et al, Ann Biomed Eng, 43/10:2456–2466, 2015
[2] Bates et al, Clinical Biomechanics, 30:1-13, 2015
[3] Bates et al, J Biomech, 53:36–44, 2017,
[4] Nesbitt et al, Am J Biomed Eng, 6/1:12–18, 2016.
[5] Herfat et al, Ann Biomed Eng, 40/7:1533-1545, 2012.
[6] Gray et al, J Orthop Res, 37:615-630, 2019.
[7] Walter et al, Med Eng Phys, 48:196-205, 2017.

IN-VITRO DENTAL IMPLANT PRIMARY STABILITY: STAIRCASE PREDICTING CONTINUOUS METHOD

Alessia Pisanu (1), Amal Saade (1), Jonas Fabech* (2), Adela Weil (2)

1. Nobel Biocare Services AG, Switzerland; 2. Zürcher Hochschule für Angewandte Wissenschaften (ZHAW), 8401 Winterthur, Switzerland

*Corresponding author: fabe@zhaw.ch, wela@zhaw.ch presenter: Adela Weil

Introduction

Primary Stability (PS) is critical for immediate loading protocols of dental implants. Fuchs et. al [1] developed a Continuous Micromotion (CM) to measure PS in-vitro. The number of cycles (n) applied significantly influences the duration of tests. Longer time often translates to higher costs for laboratories and companies. This study presents a faster method, the Staircase Method (SM), and evaluates its reliability in predicting the PS as tested in the CM method. This would contribute to significant reduction of costs and therefore increase the availability and usage of such tests.

Material and Methods

In this study, the SM was primarily developed to allow testing of implant design in Sawbone bone surrogate for a reduced n (e.g., 3’000) and at increasing load level (LL), using a stepwise approach, until reaching implant failure (IF) (Figure 1). Compared to SM, CM has a higher number of cycles (e.g., 50’000) but applied continuously at one chosen level (e.g., 100 N). Both methods evaluate two components: Migration (Mig) and Micromotion (MM) of the implant with lateral and axial movements monitored by two sensors of compressive-bending loading, during 50’000 and 3’000 cycles (n), respectively in CM and SM. MM and Mig correspond to representative relative motion between implant and surrounding material, respectively due to elastic deformation and plastic deformation of the surrogate bone. To predict CM using the faster SM values, a statistical prediction model was developed. To check the reliability of this model, out-of-sample test was performed with 4 different Nobel Biocare implant system families with different platforms and lengths (22 in total from NobelParallel, NobelReplace, Nobel Speedy, N1), tested in Sawbone of 20 pounds per cubic foot (PCF) density, and a sample size of 4. Out of the 22 implants tested in SM, 4 were tested with CM in 20 PCF (Type III bone) at 100N, and additional 4 at 140 N. Model robustness was assessed using a 2-sample T-test to compare ranking PS performances of different implant groups using the R Sofware.

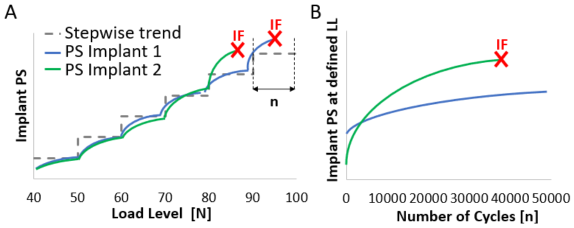

Figure 1 Sample graphs of PS in SM (A) and CM (B).

Results

The CM prediction model could predict the probability of an implant to fail at a certain LL with overall 87.5% accuracy. When assessing the model robustness, similarly high accuracy in terms of CM ranking prediction was achieved: 100% for groups tested at 100 N, 75% for groups tested at 140 N, for confidence level (CL) of 80% (Figure 2). Similarly to what arises within traditional CM testing, lower values of accuracy occur when the ranking of implants with similar performance is predicted. Thus, as presented in Figure 2, two implants tested at 140 N showed different predicted ranking (2* and 3*) compared to real data (3** and 2**). However, the prediction also showed that the endpoints of the PS curves were statistically not different (at a CL of 80%) and the same was found when comparing tested PS, proving similar performance.

Implants LL 100 N	P	R	Implants LL 140 N	P	R
NobelParallel RP 4.3 x 8.5 mm 	1	1	NobelParallel RP 4.3 x 13 mm 	1	1
NobelParallel RP 4.3 x 15 mm 	2	2	NobelReplace RP 4.3 x 11.5 mm 	2*	3**
NobelSpeedy RP 4 x 13 mm 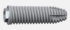	3	3	NobelReplace RP 4.3 x 16 mm 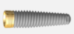	3*	2**
N1 TiUltra RP 4.0 x 11 mm 	4	4	NobelSpeedy RP 4 x 10 mm 	4	4
Accuracy CL 80% 100 N	**100 %**		**Accuracy CL 80% 140 N**	**75 %**	

Figure 2 Comparison of predicted (P) and real (R) ranking of implants tested in CM.

Discussion

This study provides evidence that SM is a reliable and robust in-vitro test that may be used as a method to predict PS faster compared with the CM method. However, how to accurately differentiate the predicted ranking of implants with similar performance remains a challenge. In additon, the accuracy ratios of the prediction might decrease when increasing the CL, or when increasing the number of compared implant groups. Future studies should further investigate the use of SM to compare implant systems.

References

1. Fuchs et al., IADR, Cape Town, South Africa; March 19-22 (2014)

Acknowledgements

We thank Stephanie Ruch, Ainara Irastorza-Landa and Maria Teresa Barletta for their support in the initiation and execution of the project. This project is funded by Nobel Biocare Services AG (R22015).

IMPACT OF SPINAL SAGITTAL ALIGNMENT AND BODY SHAPE ON SPINE BIOMECHANICS IN ADULT SPINAL DEFORMITY

Elisa R. Rosanò* (1), A. A. Hulleck (2), M. Loibl (3), T. Liu (4), M. El-Rich (2), F. Galbusera (3), F. Kleinstück (3), T. Fekete (3), D. Haschtmann (3), S. Richner-Wunderlin (3), F. Pellisé (5), I. Obeid (6), J. Pizones (7), A. Alanay (8), C. Yilgor (8), S. J. Ferguson (1), D. Ignasiak (1), ESSG European Spine Study Group

1. Institute for Biomechanics, ETH Zurich, Zurich, Switzerland; 2. Khalifa University, Abu Dhabi, UAE; 3. Schulthess Klinik, Zurich, Switzerland; 4. Ontario Tech University, Oshawa Ontario, Canada; 5. Hospital Vall d'Hebron, Barcelona, Spain; 6. Pellegrin Bordeaux University Hospital, Bordeaux, France; 7. Hospital Universitario La Paz, Madrid, Spain; 8. Acibadem University School of Medicine, Istanbul, Turkey

**Corresponding author:* erosano@student.ethz.ch

Introduction

Adult spinal deformity (ASD) encompasses disorders characterized by abnormal spinal curvature [1]. Spinal surgery for ASD aims to alleviate pain and restore global alignment, particularly in the sagittal plane [2]. High rates of mechanical complications (28-61%) suggest that alignment restoration does not always ensure optimal spinal balance (defined as trunk center of mass located over pelvis) [3] or optimal spine biomechanics without excessive loads on the spine. What is currently disregarded in the clinical consideration of spinal balance is the interpersonal variability in the body shape. Therefore, the aim of this study is to evaluate the relative effects of spinal sagittal alignment and body mass distribution along the spinal column on spinal loads and location of trunk centre of mass.

Methods

An established musculoskeletal model of the spine (AnyBody Modeling System) was used [4]. Sagittal alignment data, i.e. vertebral positions and orientations, of 831 patients with ASD was obtained from a clinical database. Trunk mass distribution data, i.e. segmental masses and centers of mass locations were assessed in a group of healthy volunteers (10 of normal weight and 9 with obesity) (Fig. 1). Inverse dynamic simulations were performed for each combination of sagittal alignment and trunk mass distribution profile to analyze spinal segmental joint reaction forces. A factorial analysis was conducted with generalized linear models to elucidate relative effects of alignment vs. body shape.

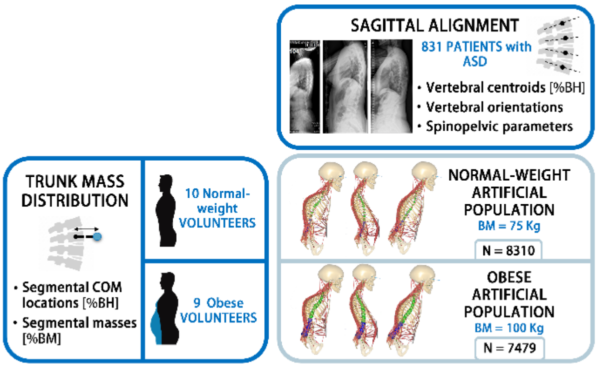

Figure 1: Simulations design: sagittal alignments of patients with ASD are assumed for each of the available measures of body mass distribution to create musculoskeletal models of two artificial patient populations in static posture (normal-weight and obese).

Results

In the simulated normal-weight population, compressive loads were largely influenced by trunk mass distribution in the lumbar region (71-77%) and to variable extent in the thoracic region (4-96%) (Fig. 2). In contrast, in the obese population, it was the sagittal alignment that had a more pronounced effect on joint reaction forces, both thoracic (60-88%) and lumbar (58-67%).

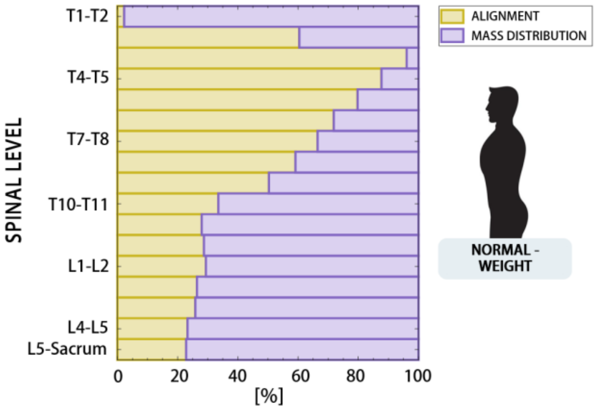

Figure 2: Relative effect of sagittal alignment and mass distribution on compressive spinal loads in normal-weight population.

Discussion

The results of this study demonstrate the considerable impact of trunk mass distribution on model-predicted spinal loads, highlighting the significance of body shape in biomechanical and clinical evaluation of ASD. Patient body shape should be considered in surgical planning for determining the amount of correction needed to maintain the trunk center of mass over the pelvis and to avoid overloading of spinal segments prone to complications. Future research should evaluate body shapes in patients with ASD, include female-specific mass distributions to reflect gender differences in body shape, and analyse dynamic tasks to account for inertial effects.

References

1. Diebo et al, The Lancet, 394(10193):160–172, 2019.
2. Glassman et al, Spine, 30(18):2024–2029, 2005.
3. Ham DW et al, Eur Spine J, 30:1190–1198, 2021.
4. Ignasiak et al, J Biomech, 49(6):959–966, 2016.
5. Liu et al, J Biomech, 122:110437, 2021.

VISCOELASTIC MATERIAL IDENTIFICATION BASED ON EXPERIMENTAL DATA USING MODEL ORDER REDUCTION

Linus Taenzer, Ivo Dobrev(2), Johannes Niermann(2), Flurin Pfiffner(2), Paolo Tiso(3), Bart Van Damme(1)

1. EMPA - Swiss Federal Laboratories for Materials Science and Technology, Dübendorf, Switzerland;
2. University Hospital Zurich, University of Zurich, Switzerland;
3. ETH Zurich, Chair in Nonlinear Dynamics, Switzerland
*Corresponding author: linus.taenzer@empa.ch

Introduction

For the development of next generation bone conduction hearing aids, numerical modeling in form of finite element simulations is becoming more and more popular. However, precise numerical modelling requires detailed material models. Bone itself exhibits both viscous and elastic properties when undergoing deformation and is therefore considered viscoelastic [1]. The identification process of viscoelastic materials can be done using nano-indentation tests [2] but it is challenging for frequencies higher than 1 kHz.

In this work, we leverage model order reduction (MOR) to determine the frequency-dependent viscoelastic properties of 3D-printed cortical cranial bone patches. These patches closely replicate the macroscale material characteristics of dry bone samples and, similar to actual bone, are composed of polymers and ceramics.

Materials and Methods

To analyze bone conduction in the frequency domain, the viscoelastic Young's modulus of bone is approximated by the fractional derivative model. This describes the complex material modulus which is used to approximate the majority of viscoelastic materials,

$$G(\omega) = \frac{G_0 + G_\infty (j\omega\tau)^\alpha}{1 + (j\omega\tau)^\alpha}, \qquad (1)$$

where G_0 is the storage modulus at 0 Hz, G_∞ is the high-frequency limit of the storage modulus, τ is the relaxation time, α is the fractional coefficient, ω is the angular frequency and j the imaginary number.

Based on Krylov subspaces, reduced order models for viscoelastic material behavior of the dynamic system are constructed [3]. The state space description is giving by

$$u = \boldsymbol{l}_{ROM}(-\omega^2 \boldsymbol{M}_{\boldsymbol{ROM}} + G(\omega)\boldsymbol{K}_{\boldsymbol{ROM}})\boldsymbol{b}_{\boldsymbol{ROM}}\hat{F} \qquad (2)$$

where u is the displacement at a single point, $\boldsymbol{l}_{ROM}$ and $\boldsymbol{b}_{\boldsymbol{ROM}}$ are the reduced selection vector of the degree of freedom used for optimization and the input point force $\hat{F}$, $\boldsymbol{M}_{\boldsymbol{ROM}}$ and $\boldsymbol{K}_{\boldsymbol{ROM}}$ are the respective stiffness and mass matrices. With the reduced order model, the four parameters of the viscoelastic material can be optimized by using particle swarm optimization, minimizing the error between frequency response functions (FRF) of the reduced order model and the Scanning Laser Doppler Vibrometer measurements, see Fig. 1.

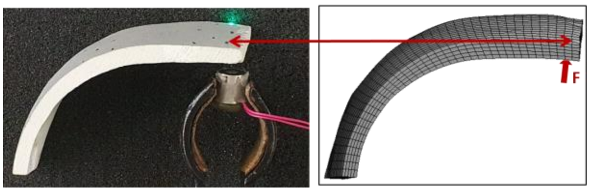

Figure 1: The material data is optimized such that the point FRF fit the experiment.

Results

With the method presented method, the material model is optimized so that the frequency dependent behavior of the actual measured sample is identified up to 7 kHz, see Fig. 2. The comparison shows errors smaller than 1% in frequency and very good agreement between the response amplitudes and damping characteristics.

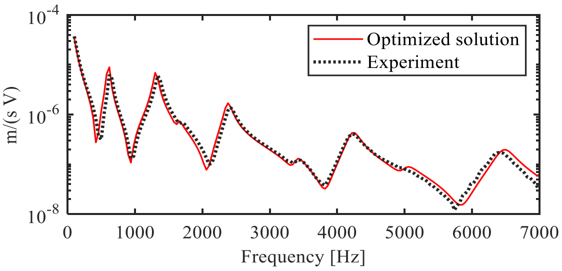

Figure 2: Modelled and measured FRF, using the optimized material properties

Discussion

The viscoelastic material identification scheme presented in this work is used for single material bone patches. However cranial bone is a composite material with a porous midlayer. For future work, optimizing the behavior of different materials simultaneously would be needed.

References

1. J. D. Currey, *Bones: Structure and Mechanics.* Princeton, 2013.
2. Do-Gyoon et al, Handbook of Nanomaterials Properties, 41:1321-1341, 2014.
3. Xie et al, CMAME, 2018

Acknowledgements

This work was supported by SNF grant 213127.

EVALUATION OF A NEW COLLECTION TECHNIQUE FOR TOUCH DNA: THE DNA-BUSTER

J. Währer[1], S. Kehm[1], M. Allen[2], L. Brauer[2], O. Eidam[3], I. Seiberle[1], S. Kron[1],
E. Scheurer[1], I. Schulz[1]

[1]Universität Basel, Department of Forensic Genetics, Institute of Forensic Medicine, Switzerland
[2]Department of Immunology, Genetics and Pathology, University of Uppsala, Sweden
[3]OTR-Performance GmbH, Cologne, Germany

*Corresponding author: iris.schulz@bs.ch, presenter: Janine Schulte

Introduction

Biological material is often secured as potential evidence for crime investigations by rubbing with swabs or taping. One common trace type is touch DNA (85% of the traces, [1]), i.e., biological material transferred from a person to an object via contact [2]. Touch DNA, however, is challenging to secure due to its extremely low DNA quantity, poor quality, operator's "blind" sampling and risk of contamination. Further, since current research indicates an interaction between substrate properties and collection methods, research efforts are focusing on developing new and effective collection techniques, such as suctioning [3,4]. At the Institute of Forensic Medicine Basel, Switzerland, the DNA-Buster has been developed, a new dry suction device for forensic use. It is mobile and can be used both stationary and on the crime scene, allowing access to hard-to-reach areas like crevices or vehicle seats (Fig. 1, [4]).

Material and Methods

In this study, an in-house dry-vacuuming device, the DNA-Buster, was developed, technically optimized, and compared to traditional methods for its DNA recovery performance (i.e., DNA yield and profile quality) from items typically examined in forensic casework. The aim was to evaluate the effectiveness of this dry-vacuuming approach in recovering DNA efficiently, potentially complementing the well-established recovery strategies. For this, the performances of swabbing, taping, wet- (M-Vac®), and dry-vacuuming (DNA-Buster) were investigated quantitatively and qualitatively for touch DNA deposited on five different substrates (i.e., carpet, cotton sweater, stone, tile, and wood).

Results and Discussion

Firstly, the results prove the DNA-Buster to be superior for securing touch DNA from textiles (Fig. 2). Hence, enhanced DNA recovery from fabric material could improve the criminal clearance rate by 7 % (~ 36'500 victims in 2023, [5]). Secondly, the need for optimization is shown when utilizing it on other substrates, as conventional methods outperform on wood and stone. Thirdly, the data emphasize the dependence of the collection method and the substrate. Therefore, the results provide essential insights for determining the optimal method for the precise and targeted collection of genetic material from forensic traces. Next steps will address the device's technical optimization, such as improving the filter tips, filter characteristics, and pumps/airflow to ensure DNA recovery broadened for substrates beyond textiles.

Figures and Tables

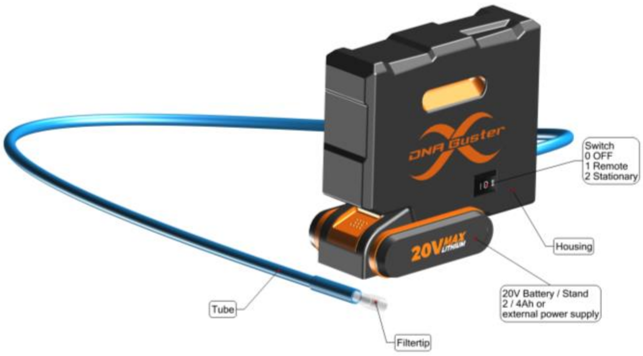

Figure 1: CAD model of the DNA-Buster v3.

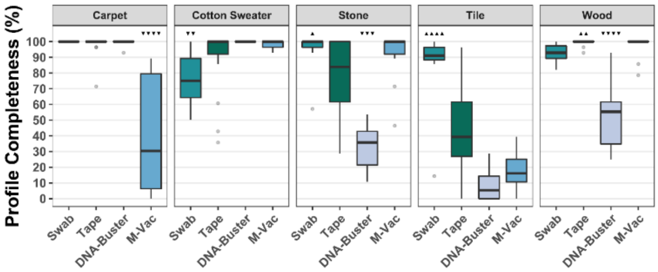

Figure 2: STR profile results. Boxplots show the completeness of DNA profiles per sampling method for the five surfaces examined. Arrows pointing up indicate significantly higher results, and arrows pointing down significantly lower results.

References

1. Comte et al, Forensic Sci Int Genet., 43:102113, 2019.
2. Tozzo et al, Int J Mol Sci., 23(24): 15541, 2022.
3. Kaesler et al, Forensic Sci Int., 348 : 111728, 2023.
4. Währer et al, Forensic Sci Int Genet, 64: 102830, 2023.
5. Internal communication with M. Girardin, Deputy Head of Forensics Department, Police Solothurn, statistics from 10.02.2020. This number is supported by the commissioned work of three cantonal police customers (BS, BL and SO) within the Laboratory Management System of the Department of Forensic Genetic, IRM Basel.

TRANSFORMING CLINICAL ASSESSMENTS: RATER RELIABILITY IN VIDEO-BASED EVALUATION OF UPPER EXTREMITY AFTER STROKE

Lena Sauerzopf* (1,2), Celina G. Chavez Panduro (3), Andreas R. Luft (4), Benjamin Kühnis (5), Elena Gavagnin (5,6), Tim Unger (7,8), Chris Easthope Awai (7), Josef G. Schönhammer (4), Jürgen Degenfellner (9), Martina R. Spiess (1)

1. ZHAW School of Health Sciences, Institute of Occupational Therapy, Switzerland; 2. Faculty of Medicine, University of Zurich, Switzerland; 3. University for Continuing Education Krems, Austria; 4. Neuroscience of Motivation and Cognition in Rehabilitation (NeuroCoRe) Lab University of Zurich and University Hospital Zurich, Switzerland; 5. ZHAW Zurich University of Applied Sciences, Institute of Business Information Technology; 6. ZHAW Zurich University of Applied Sciences, Centre for Artificial Intelligence; 7. Data Analytics and Rehabilitation Technology (DART) Lab, Lake Lucerne Institute, Switzerland; 8. Rehabilitation Engineering Laboratory, ETH Zurich, Switzerland; 9. ZHAW School of Health Sciences, Institute of Physiotherapy, Switzerland

**Corresponding author:* lena.sauerzopf@zhaw.ch, Lena Sauerzopf and Celina G. Chavez Panduro equally contributed to this work.

Introduction

Compensatory movements often occur during motor recovery following a stroke and lead to negative long-term consequences [1] (see Figure 1). Deep learning methods have demonstrated promising potential for evaluating movement quality [2].

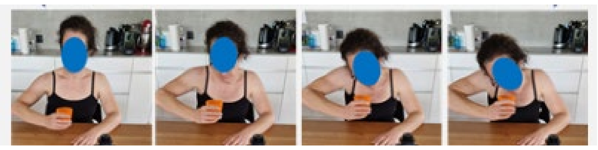

Figure 1: Able-bodied person simulating compensation through trunk and shoulder during the drinking task.

However, to create a valid ground truth based on therapist's assessment of compensatory movements, reliability of these ratings must be ensured. This study aimed to evaluate the reliability of therapists' visual assessments of compensatory movements using 2D-video analysis.

Material and Methods

Twenty-two occupational and physical therapists evaluated video recordings showing a standardized drinking task performed by seven patients after stroke using an online system (scale from 0 = no compensation to 100 = max. compensation). We analyzed data using a generalized-linear mixed effects model with zero-inflated beta regression [3].

Results

Our cohort demonstrated moderate to excellent reliability for the phases of reaching, drinking, and returning, and poor reliability for smoothness and interjoint coordination (see Table 1.). Wide Credible Intervals for the ICCs across all measured domains demonstrate high degree of uncertainty. Examples of high and low agreement between the raters are shown in Figure 2.

Discussion

We propose three approaches to overcome the issue of difficulties in conducting video analysis: increasing the sample size of raters (1), providing therapists with training for calibration on key metrics of compensatory movements and the labeling system (2), and integrating additional kinematic motion analysis technologies (3).

Table 1: Overview Results

Movement	ICC (95% CI) Inter-rater	ICC (95%) Intra-rater
Reaching	0.76 (0.44-1)	0.73 (0.22-1)
Forward Transport	0.68 (0.38-1)	0.84 (0.20-1)
Drinking	0.88 (0.60-1)	1 (0.24-1)
Back Transport	0.65 (0.31-1)	0.67 (0.18-1)
Returning	0.75 (0.43-1)	0.76 (0.21-1)
Global		
Smoothness	0.49 (0.18-1)	0.13 (0.02-0.86)
Interjoint Coordination	0.40 (0.13-1)	0.19 (0.03-1)

ICC= Intraclass Correlation, CI = Credible Interval

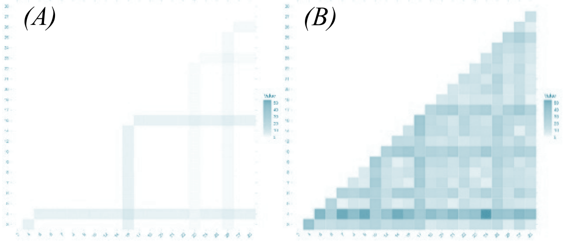

Figure 2: (A) High Agreement (combination fingers/grasp/reach: min. absolute difference of 0 and max. 7.77). (B) Low Agreement (combination body region/movement/phases: minimum mean 0 and max. 54.14)

References

1. Levin MF, Kleim JA, Wolf SL. What Do Motor "Recovery" and "Compensation" Mean in Patients Following Stroke? Neurorehabil Neural Repair. Mai 2009;23(4):313–9.
2. Mennella C, Maniscalco U, Pietro GD, Esposito M. A deep learning system to monitor and assess rehabilitation exercises in home-based remote and unsupervised conditions. Computers in Biology and Medicine. 1. November 2023;166:107485.
3. Bürkner PC. brms: An R Package for Bayesian Multilevel Models Using Stanbürkner. J Stat Soft [Internet]. 2017 [zitiert 16. Juni 2024];80(1). Verfügbar unter: http://www.jstatsoft.org/v80/i01/

Acknowledgement

This work was supported by DFF Futures Fund (ZHAW Digital).

µCT IMAGES FROM CLINICAL CT OF THE HUMAN PROXIMAL FEMUR USING DEEP LEARNING

Osman Berk Satir (1), Simon Gremaud (1), Gabriela Gerber (1), Pezhman Eghbali (2), Fabio Becce (3), Patrick Goetti (3), Alexandre Terrier (2, 3), Philippe Büchler (1)

1. ARTORG Center for Biomedical Engineering Research, Switzerland; 2. Ecole Polytechnique Fédérale de Lausanne (EPFL), Switzerland; 3. Lausanne University Hospital (CHUV), Switzerland

*Corresponding author: osman.satir@unibe.ch

Introduction

Image-based modeling is widely used for personalized biomechanical simulations. Previous studies have shown that bone strength can be accurately estimated from bone mineral density (BMD) and trabecular bone structure. However, calibrated clinical CT scans only provide BMD values and do not capture trabecular bone structure, limiting the accuracy of numerical models for clinical applications such as diagnostics, implant design, or surgical planning. To bridge this gap, we have developed a method that uses generative adversarial networks (GAN) to effectively reconstruct µCT images (high-resolution) from clinical CT scans (low-resolution).

Material and Methods

Our dataset consisted of 58 calibrated and downsampled µCT scans of the human proximal femur (34.2x34.2x34.2 µm) and the corresponding calibrated clinical CT scans (0.5x0.5x0.5 mm). Since the high-resolution (HR) and low-resolution (LR) scans were acquired with different scanners, the scans were initially registered. 87000 corresponding 3D patches were randomly extracted from the whole dataset of LR (16x16x16) and HR (64x64x64) scans, with an upsampling factor of 4. 69600 of the extracted patches were used to train the generative adversarial network (GAN), which used the LR scan as input and generated the super-resolution (SR) scan. The rest of the patches were used for validation. We evaluated the quality of the generated SR scans by visually comparing them with their corresponding HR scans. We also quantified various bone structure properties, such as bone volume fraction (BV/TV) and degree of anisotropy (DA) from both the original HR and generated SR scans.

Results

Visual observation of different corresponding patches from the original LR and HR images, as well as from the generated SR image, shows that the model can learn the microstructure information and is able to generate higher-resolution images (Figure 1). The BV/TV of the patches extracted from the generated SR and original HR scans correlated very well (r=0.98). However, a weaker correlation was observed between SR and HR for the DA of the local patches (r=0.43), and the DA from the generated SR scans tended to underestimate the DA of the corresponding patches of the original HR scans (Figure 2).

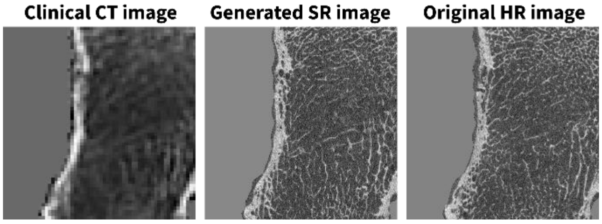

Figure 1: An example slice from clinical CT scan (a), the correspondent generated SR image (b) and the original HR image (c)

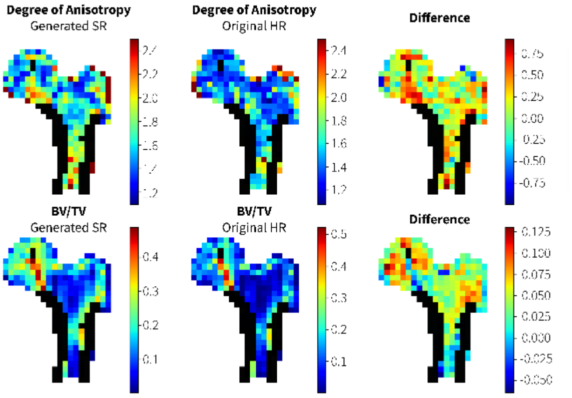

Figure 2: Bone structural properties obtained from generated SR and original HR scans. Rows represent the DA and BV/TV of the generated SR and original HR scan, and their difference. BV/TV was similar, whereas DA was consistently lower in the generated SR scans.

Discussion

In this study, we proposed using a GAN-based architecture to generate high-resolution CT scans from clinical CT scans. While the BV/TV of the generated SR scans correlated well with the HR scans, the DAs of the patches obtained from the SR scans were consistently lower than the corresponding patches in the HR scans. Since the structures generated in the SR images were thinner than in the HR scans, they might have a higher variability in orientation, leading to an overall decrease in DA. Further mechanical evaluation should be performed to understand whether including DA information extracted from the generated SR scans can improve the predictions for mechanical simulations. Future work will explore predicting the microstructure directly from the clinical CT scans.

Acknowledgements

This work is supported by the Swiss National Science Foundation (Grant no: 189972).

BONE CONDUCTION HEARING: METHODS FOR THE VALIDATION OF COMPUTATIONAL MODELS

Johannes Niermann* (1), Ivo Dobrev (1), Linus Taenzer (2), Tobias Mair (1), Bart Van Damme (2), Christof Röösli (1), and Flurin Pfiffner (1)

1. *Department of Otorhinolaryngology, Head&Neck Surgery, University Hospital Zurich, University of Zurich, Switzerland*
2. *EMPA - Swiss Federal Laboratories for Materials Science and Technology, Dübendorf, Switzerland*

*Corresponding author: Johannes.Niermann@usz.ch

Introduction

Bone conduction hearing aids (BCHA) can be used for patients with conductive and mixed hearing loss or single-sided deafness. The transfer path of the BCHA stimulus to the cochlea is very complex, due to the material properties of bone, the fluid-structure interaction, and the dispersive elastic wave propagation that depends on the skull's geometry.

Efficient and accurate numerical models would represent a leap forward in the understanding of bone conduction (BC) and enable the development of BCHA for personalized treatment. Objective validation techniques are a prerequisite to judge the quality of a BC model’s predictions. This work aims to present recent developments in our validation methods for computational models (CMs) in BC hearing.

Material and Methods

To obtain the most realistic results, the measured samples were fresh cadaver heads or specific pieces of the skull. CT-scans were being used to create model geometries and register measurement data. We measured the frequency dependent complex surface motion (SM) of the skull at predefined points with a SWIR Scanning Laser-Doppler-Vibrometer (SLDV, Optomet GmbH, Germany). These recordings were done using various BC excitations, e.g. BCHA or electromagnets [1, 2]. The resulting SM grid was interpolated and compared with results from an existing BC CM of a head.

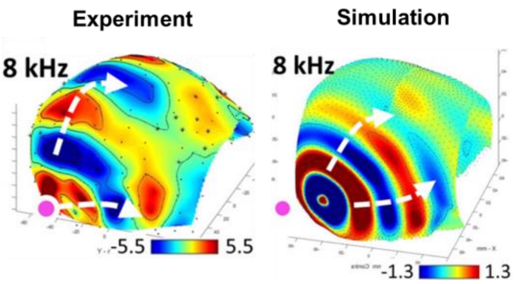

Figure 1: Mode shape correlation of measurement data (left) and CM data (right) at the same frequency for two different heads [1].

Results

We have shown good qualitative correlation of wave motion between our interpolated SM data and data from the existing BC CM of a head at multiple frequencies up to 10 kHz (Fig. 1).

Recent preliminary studies showed promising results for an automized spatial cross-correlation of mode shapes of bone pieces with simulation geometries from CT scans (Fig. 2). With a simple linear elastic model, a modal assurance criterion of 0.8 could be achieved in the same frequency range up to 10 kHz.

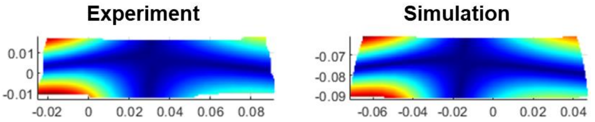

Figure 2: Mode shape correlation of measurement data at 1490 Hz (left) and CM data (right) for the same mode of the same bone piece.

Discussion and Outlook

A manual qualitative correlation of experimental SM data and computational results with different geometries can be a valid method for proof-of-concept studies. However, relying on a single reference model geometry for a head lacks the necessary detail and generalization needed to develop an accurate CM for BC. Using the same geometry in experiment and simulation helps going beyond qualitative comparisons.

Automation methods for correlating mode shapes between experimental data and CM could speed up and improve the validation process. The apparent validation errors could be eliminated by carefully modelling the frequency-dependent viscoelastic material properties, further aligning boundary conditions and excitation in both experiment and CM, and paying special attention to the registration of experimental data and coordinate transformations between experimental data and simulation data.

References

1. Dobrev et al, J Acoust Soc Am, 1985–2001, 2020.
2. Farahmandi et al, J Acoust Soc Am, 1593–1606, 2022.

Acknowledgements

This research is supported by SNF grants Nr. 188740 and Nr. 213127.

INTRAVITAL IMAGING OF THE MOUSE CENTRAL NERVOUS SYSTEM FLUID SPACES USING SYNCHROTRON COMPUTED TOMOGRAPHY

Marta Girona Alarcón (1), Willy Kuo (1), Britta Bausch (1), Mattia Humbel (2), Irene Spera (3), Luca Fardin (4), Hans Deyhle (2), Christine Tanner (2), Petr Pleskač (3), Anastasia Çakmak (1), Britta Engelhardt (3), Steven T. Proulx (3), Bert Müller (2) and Vartan Kurtcuoglu* (1)

1. Institute of Physiology, University of Zurich, Switzerland; 2. Biomaterials Science Center, University of Basel, Switzerland; 3. Theodor Kocher Institute, University of Bern, Switzerland; 4. Department of Medical Physics and Biomedical Engineering, University College London, UK

*Corresponding author: vartan.kurtcuoglu@uzh.ch

Introduction

Computational fluid dynamics (CFD) based on anatomy data obtained by *in vivo* magnetic resonance imaging (MRI) is a powerful tool for studying cerebrospinal fluid (CSF) dynamics and associated transport processes in humans. For acquiring the mouse central nervous system (CNS) fluid space anatomy, MRI is not the ideal modality because of its limitations in resolution and signal-to-noise ratio. In contrast, intravital multi-photon fluorescent microscopy offers high resolution, but limited field of view and penetration depth, making it unsuitable for whole-organ CFD studies of CSF dynamics. To address the shortcomings of these established imaging modalities, we have developed a pipeline for intravital whole mouse brain imaging at 8 µm voxel size using synchrotron radiation-based hard X-ray micro computed tomography (SRµCT).

Material and Methods

The general imaging setup is shown in Fig. 1. Anesthetized C57BL/6J mice were outfitted with a ventricular infusion cannula and a tracheal cannula. They were placed in upright position in a custom-designed heated holder mounted on a precision rotation stage. Anaesthesia was maintained by admixing of isoflurane to the oxygen-enriched air supplied by a ventilator. Vital signs were monitored by electrocardiography (ECG), pulse oximetry, capnography, and rectal temperature measurement. 5 µl of a barium-based nanoparticle contrast agent were infused into one of the lateral ventricles at 0.25 µl/min. SRµCT was performed at the beamlines ID17, BL20B2, and BMIT of the European Synchrotron Radiation Facility (ESRF), the Super Photon Ring – 8 GeV (SPring-8), and the Canadian Light Source (CLS), respectively. Imaging and other experimental parameters were varied in the method development process.

Results and Discussion

Cerebral ventricles were clearly delineated by the contrast agent, enabling efficient semi-automatic segmentation. The high image resolution and contrast also permitted labelling of the choroid plexus. However, for precise segmentation along the latter's convoluted surface, higher resolution would be necessary. Time-resolved acquisitions showed the progression of contrast agent distribution also in the subarachnoid space. These data could be used to quantify the CSF velocity by solving the inverse problem. ECG-gated acquisitions allowed the detection of periodic tissue motion outside the skull. We were not able to detect brain motion induced by cardiorespiratory action. It is unclear whether this was due to insufficient spatial resolution and/or signal-to-noise ratio, other technical limitations, or whether brain motion is negligibly small in the mouse. Time-resolved *peri-mortem* acquisitions showed a gradual reduction of ventricular volume, as well as a shift in the position of the choroid plexus, confirming the need for in *vivo* acquisition of CNS fluid space geometry for subsequent CFD analysis.

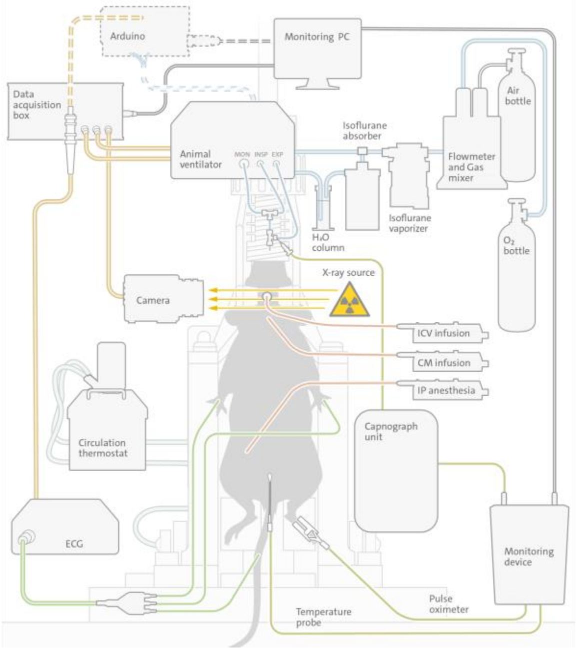

Figure 1: Illustration of experimental setup. ICV: ventricular. CM: cisternal. IP: peritoneal. The mouse is placed on a rotation stage for imaging by SRµCT.

Acknowledgements

SRµCT was performed at the beamlines ID17, BL20B2, and BMIT of ESRF, SPring-8, and the CLS, respectively. Imaging and other experimental parameters were varied in the method development process.

A TOMOGRAPHY SLICE THROUGH THE ENTIRE HUMAN BRAIN WITH LESS THAN THREE MICROMETER VOXELS

Mattia Humbel* (1), Felix Beckmann (2), Julian Moosmann (2), Hans Deyhle (1), Georg Schulz (1,3), Christine Tanner (1,3), Griffin Rodgers (1), Bert Müller (1)

1. Biomaterials Science Center, University of Basel, Allschwil, Switzerland;
2. Institute of Materials Physics, Helmholtz-Zentrum Hereon, Geesthacht, Germany;
3. Core Facility Micro- and Nanotomography (MiNa), University of Basel, Allschwil, Switzerland
*Corresponding author: mattia.humbel@unibas.ch

Introduction

The gold standard techniques for imaging the human brain with cellular resolution rely on serial sections [1, 2], potentially sacrificing out-of-plane resolution and introducing slicing artefacts. X-ray microtomography has the potential to offer isotropic (sub-)cellular resolution without the need for physical sectioning. It has been used to image the entire brain at 25 µm voxel size, and selected regions at 6 µm [3]. In this study, we present the acquisition and reconstruction of a 2 mm high and 11.5 cm wide virtual section of the human brain with 2.54 µm voxels.

Material and Methods

An adult human brain was fixated in formalin, dehydrated, and immersed in 100% ethanol for tomographic imaging. The P07 beamline at DESY, Hamburg, Germany, operated by Helmholtz-Zentrum Hereon, Geesthacht, Germany, was configured to produce a monochromatic 67 keV X-ray beam. The specimen was placed on a rotation stage 80 cm away from the detector array, to exploit propagation-based phase contrast. Using a 5× magnifying lens led to $(1.27\ \mu m)^2$ effective pixel size. To cover the entire 11.5 cm wide specimen with the 6.5 mm detector field-of-view (FOV), the projected area had to be extended 20 times laterally. This extended FOV was achieved by acquiring ten rings with the specimen offset with respect to the rotation axis, each ring consisting of 48’000 projections over 360°. The exposure time was 30 ms per projection. The partial projections were stitched and superimposed using the pixel-precise motor position prior to tomographic reconstruction.

Results

A single reconstructed slice with 2× binning measures 45’403 × 45’403 voxels, occupying 7.7 GB of storage at 32-bit precision. The acquisition of one height step in fly-scan mode took 4.5 hours. Figure 1 shows an exemplary coronal slice.

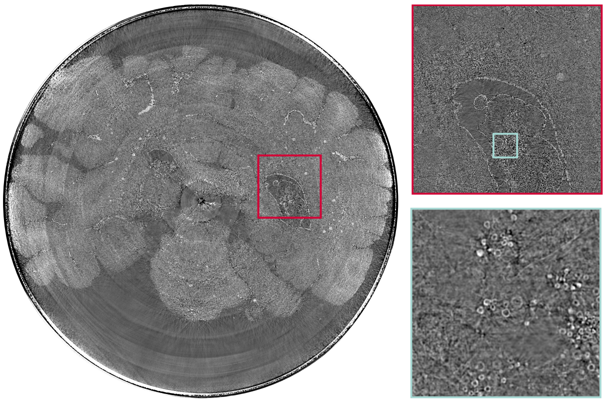

Figure 1: Tomographic slice through the human brain with 2.54 µm voxels. Left: Scan covers the entire 11.5 cm specimen. Right: Zoom-ins demonstrate the full resolution. The size of the red box is 18.8 mm, of the mint-colored one 2.5 mm.

Discussion

This synchrotron radiation-based study shows the feasibility of employing X-ray tomography to image the entire human brain using isotropic voxels 2.54 µm wide. In a next step, several 10’000 slices, each several GB in size, must be tiled vertically, posing the challenge of handling the big data of an entire human brain with PB size and providing access to the research community.

References

1. Amunts et al, Science, 340:1472-1475, 2013.
2. Ding et al, J Comp Neurol, 524: 3127-3481, 2016.
3. Walsh et al, Nat Methods, 18:1532-1541, 2021.

Acknowledgments

The authors thank Prof. Magdalena Müller-Gerbl, University of Basel, Switzerland for providing the specimen. This work was supported by grant 185058 from the Swiss National Science Foundation. We acknowledge DESY, Hamburg, Germany for the provision of experimental facilities. Beamtime at PETRA III, P07 beamline, operated by Helmholtz-Zentrum Hereon, Geesthacht, Germany, was allocated for proposals 20221154 and 20230593.

AUTOMATING GROUND TRUTH MASK GENERATION FOR LOW-CONTRAST CT PHANTOM SCANS

Marco Mathys* (1), David Stocker (1), Mathias S. Weyland (1), Stephan Scheidegger (1)

1. *ZHAW School of Engineering, 8401 Winterthur, Switzerland*

*Corresponding author: mathyma1@students.zhaw.ch

Introduction

In evaluating Computed Tomography (CT) scans for protocol and safety optimization, it is critical to balance radiation dose and image quality. The Difference Detail Curve (DDC) method offers a realistic assessment of image quality by determining the smallest detectable contrast difference using low-contrast objects in specialized phantoms. [1] To evaluate DDCs, it is essential to utilize precise ground truth masks delineating specific contrast objects. Traditionally, this labor-intensive process requires meticulous human input.

Ground truth masks are essential for training Model Observers (MO), as they provide reference data against which the models' predictions can be compared and refined. MO, computational algorithms that mimic human performance in assessing medical images, automate and standardize the evaluation process, ensuring consistent and objective assessments. [2]

The anticipated acceleration of the evaluation process is expected to result from the automation of Ground Truth mask generation and alignment using the Segment Anything Model (SAM). A graphical user interface (GUI) is employed to create an initial mask for each phantom using high-dose CT scans, which are then aligned using image registration techniques combined with SAM. This method accounts for different phantoms with varying sizes and placements of low-contrast objects. The project aims to examine the minimum dosage and maximum slice thickness necessary for robust results, enhancing the reliability and efficiency of DDC evaluations.

Material and Methods

Sommer et al. [3] developed a range of phantoms to simulate different body parts, such as the head and abdomen. These phantoms feature low-contrast inlets, the visibility of which is assessed to generate DDCs for specific scan protocols. A React-based GUI leverages SAM's interactive segmentation capabilities, enabling users to create masks with ease. This involves selecting areas to include or exclude and making fine adjustments. A fitting algorithm then transfers these ground truth masks from high-dose scans to new scans. Specifically, to obtain an initial orientation, the three-dimensional mask is spatially aligned by applying image registration (see Figure 1). The fine adjustments of the DDC inlays can be made based on the features extracted by Zero-Shot Segmentation. The quality of the alignment is evaluated using the Intersection over Union (IoU) metric. Testing was conducted to ensure robustness across varying image qualities, with particular attention paid to high noise or low dose.

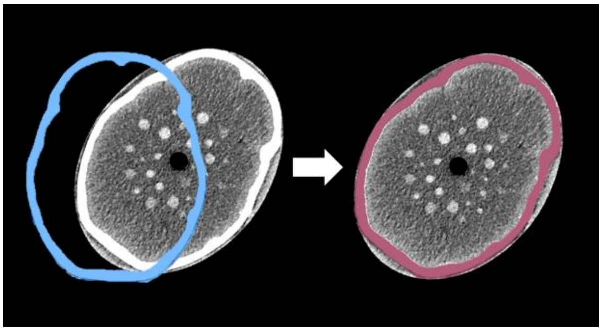

Figure 1: Schematic representation of the image registration of the head phantom. The orientation of a new CT scan can be determined by aligning the initial mask (blue) and obtaining a transformed mask (red).

Results

The developed method demonstrated robustness and efficiency in generating and aligning ground truth masks to new CT scans.

The intuitive GUI enabled users to swiftly select regions of interest, leveraging SAM's powerful backend application. This process ensured accurate and reliable alignment of masks, even in the presence of significant noise and varying orientations. The distinct low-contrast objects within the phantoms facilitated precise alignment of the inlay module, confirming the method's effectiveness in diverse conditions.

Discussion and Conclusion

The automated approach with the GUI and the image registration algorithm has reduced the effort required to create the initial ground truth mask and consequently also the fitting to new CT scans. This has significantly improved the efficiency of mask alignment by ensuring accurate identification and positioning of low-contrast objects. There are plans to extend the pipeline to other phantoms, recognizing that different anatomical regions require unique features and characteristics. While the basic process remains consistent, each phantom will be adapted to its specific characteristics. This adaptability underlines the potential for broad application, increasing the reliability of DDC evaluations in different clinical scenarios. Furthermore, should new phantoms be developed, this approach should be readily adaptable to accommodate their distinctive characteristics.

References

1. Sommer et al, 2017, CDBME, 3(2), 517–519
2. Stocker et al, 2024, Phys. Med. Biol., 69, 115026
3. Sommer et al, 2022, ZMP, 32(2), 209–217

MICRON-RESOLUTION IMAGING OF PALATAL ANATOMY WITH COMPUTED TOMOGRAPHY

Daphne Schönegg* (1, 2), Hans Deyhle (1), Christine Tanner (1), Andreas A. Müller (3, 4), Magdalena Müller-Gerbl (5), Georg Schulz (1, 6) and Bert Müller (1)

1. Biomaterials Science Center, Department of Biomedical Engineering, University of Basel, Switzerland
2. Department of Cranio-Maxillofacial Surgery, Bern University Hospital (Inselspital), Switzerland
3. Department of Oral and Craniomaxillofacial Surgery, University Hospital Basel
and University Children's Hospital Basel, Switzerland
4. Facial and Cranial Anomalies Research Group, Department of Biomedical Engineering
and Department of Clinical Research, University of Basel, Switzerland
5. Anatomical Institute, University of Basel, Switzerland
6. Core Facility Micro- and Nanotomography, Department of Biomedical Engineering, University of Basel, Switzerland

*Corresponding author: daphne.schoenegg@insel.ch

Introduction

Optimal handling of the pterygoid hamulus and adjacent soft tissues (tensor veli palatini muscle and palatal aponeurosis) during palatoplasty in infants with cleft palate remains controversial, primarily because the micro-anatomy of this region and resulting functional implications are not yet fully understood.

Micro-computed tomography (μCT) is recognized as a non-destructive imaging method capable of visualizing anatomical structures at resolutions comparable to conventional histology [1, 2]. Its potential to visualize palatal muscles has been demonstrated in iodine-stained fetal specimens [3, 4]. This study aimed to elucidate the three-dimensional topographic relationships between the pterygoid hamulus and its surrounding tissues in an un-stained specimen.

Material and Methods

The right half of a historical plastinated infant head obtained from the Institute of Anatomy at the University of Basel was studied.

Two laboratory-based μCT systems were used for data acquisition. The entire specimen was imaged with the phoenix|xray nanotom® m. High-resolution local tomography of the region of interest was performed with the Zeiss Xradia 610 Versa. Two-dimensional images were reconstructed with the respective manufacturer's software and subsequently exported for segmentation in VGStudio MAX and ImageJ.

Table 1: Data acquisition parameters.

parameters	nanotom® m	Xradia 610 Versa
acceleration voltage [kV]	170	110
beam current [μA]	30	141
pixel size [μm]	55	3.4
no. of projections	1800	6001
exposure time [s]	18	25

Results

The tomographic images revealed distinct features in both hard and soft tissues. Differentiation between muscle and aponeurosis was not feasible due to similar contrast characteristics in the plastinated specimen. Nonetheless, segmentation based on fiber direction enabled a three-dimensional visualization of the region surrounding the pterygoid hamulus.

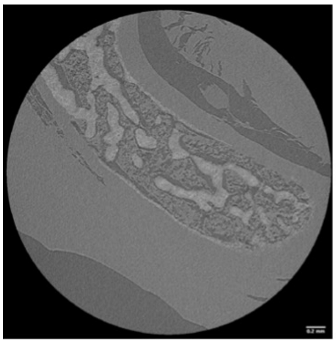

Figure 1: High-resolution visualization of the pterygoid hamulus and adjacent muscles (Xradia 610 Versa).

Discussion

The findings support the hypothesis that the tensor veli palatini muscle and its extension into the palatal aponeurosis form a muscle sling around the pterygoid hamulus, with the superior pharyngeal constrictor muscle attaching further posteriorly. Laboratory-based μCT proved suitable for high-resolution imaging of hard and soft tissues in a plastinated specimen.

References

1. Khimchenko A et al, Neuroimage, 139:26-36, 2016.
2. Holme MN et al, Nat Protoc, 9(6):1401-15, 2014.
3. Zhao J et al, Cleft Palate Craniofac J, 60(3):319-326, 2023.
4. Di W et al, Plast Reconstr Surg, 148(3):389e-397e, 2021.

Acknowledgements

The authors thank Dr. Szilvia Mezey (Anatomical Institute, University of Basel) for her support with specimen selection.

PHOTON-COUNTING CT: A COMPARATIVE STUDY FOR BONE VOLUME FRACTION MEASUREMENT

Patrik Wili (1,2), Dominic Gascho* (1), Philippe Zysset (2)

1. Institute of Forensic Medicine, University of Zurich, Switzerland; 2. ARTORG Centre for Biomedical Engineering Research, University of Bern, Bern, Switzerland

*Corresponding author: dominic.gascho@uzh.ch

Introduction

The assessment of bone density is crucial for the diagnosis of bone diseases such as osteoporosis. Traditional methods such as quantitative computed tomography (QCT) quantify bone mineral density (BMD) and bone volume/total volume (BV/TV). These parameters predict bone strength but require calibration phantoms and are affected by soft tissue variations. New spectral CT technologies such as photon counting CT (PCT) are promising for a different approach. They may allow phantomless BV/TV quantification, which may reduce radiation dose and reduce the influence of soft tissue on measurements.

This study aims to compare how conventional dual-energy CT (DECT) and advanced PCT handle soft tissue variations in BV/TV measurements compared to conventional QCT measurements. We hypothesize that the phantomless approach of DECT and PCT reduces soft tissue bias, allowing for more accurate and, especially when using PCT, lower-dose bone assessments. This could improve osteoporosis screening and bone monitoring.

Material and Methods

This study investigated the impact of soft tissue variations on BV/TV measurements using micro-CT (µCT) as the gold standard. Sixteen cylindrical trabecular bone biopsies from bovine tibias underwent CT scans with µCT, QCT, DECT, and PCT. Scans included air, saline, and fat substitutes to simulate bone marrow variations. All scans except DECT and PCT used a calibration phantom. DECT and PCT employed virtual monochromatic images (VMI) for analysis, potentially reducing bias from soft tissue composition. Statistical comparisons assessed how each CT method handles soft tissue variations compared to µCT.

Equations

HU values exhibit a strong dependency on energy level E. Utilizing VMIs enables the direct computation of BV/TV through a designated system of equations.

$$HU(E) = \sum_{i=component} \rho_i \alpha(E)_i \phi_i - \Theta$$

ϕ_i volume fraction, ρ_i density, $\alpha(E)_i$ energy dependent CT coefficient of component i, Θ HU shift (-1000 HU)

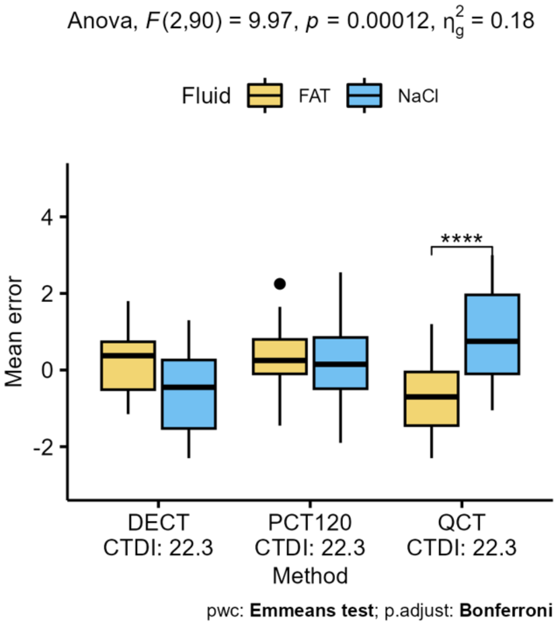

Figure 1: Boxplot of me grouped by the BV/TV method and fluid. A high difference can be seen between NaCl and fat for QCT. No differences could be found for DECT and PCT.

Nickoloff et al. (1988)[1] adapted this equation for trabecular bone by leveraging its composition of collagen, calcium hydroxyapatite, water, red marrow, and adipose tissue.

References

1. Nickoloff EL, Feldman F, Atherton JV. Bone mineral assessment: new dual-energy CT approach. Radiology. 1988;168(1):223-228. doi:10.1148/radiology.168.1.3380964
2.

Acknowledgements

Acknowledgements are not mandatory.
We thank Alice Dudle, Roy P. Marcus, Daniel Nanz, Michael Thali for the additional review of the final manuscript and the provision of scan units.

SIMULTANEOUS ELECTROENCEPHALOGRAPHY AND FUNCTIONAL MAGNETIC RESONANCE IMAGING AT 7 TESLA: HUMAN EVALUATION

Cristina Sainz Martinez (1), Jonathan Wirsich (2), Serge Vulliémoz (2), Mathieu Lemay (1), Jessica Bastiaansen (4), Roland Wiest (5), João Jorge* (1)

1. CSEM - Swiss Center for Electronics and Microtechnology; 2. Dept. of Clinical Neurosciences, University Hospitals of Geneva; 4. Dept. of Diagnostic, Interventional and Pediatric Radiology, Bern University Hospital; 5. Inst. of Diagnostic and Interventional Neuroradiology, Bern University Hospital; Switzerland

*Corresponding author: joao.jorge@csem.ch

Introduction

Functional MRI (fMRI) can be well complemented by scalp electroencephalography (EEG), which has lower spatial, but higher temporal specificity. The application of this multimodal technique at 7 Tesla, boosting the sensitivity of fMRI, could unlock new opportunities to study brain function and dysfunction, e.g. in cortical layer connectivity. However, when combined, EEG and MRI interfere with each other, creating strong artifacts that increase with field strength, and physical constraints that prevent the use of dense receive RF arrays for MRI. To tackle these challenges, we implemented a 7T EEG-fMRI framework combining, for the first time, several key advances from recent studies: (i) compact EEG setup to minimize artifact induction [1], (ii) integrated artifact sensors to denoise the EEG [2], and (iii) EEG lead adaptations to allow its combination with a state-of-the-art 32ch-receive RF array [3]. The new setup was extensively characterized in a phantom and in humans, including fMRI protocols with sub-mm resolution.

Methods

Setup: 7T Terra MRI (Siemens) with a 32ch-receive head RF coil (Nova), and an MR-compatible 64ch EEG system (Brain Products), where the cap was adapted to fit in the RF coil, similar to [3]. The amplifiers were placed just behind the coil, to minimize cable lengths [1]. Four electrodes were converted into artifact sensors [2]. Temperature probes were added to monitor heating.
Data acquisition: Included a phantom and 8 healthy adults, with ethics approval and informed consent. Each participant underwent acquisitions with MRI only, EEG only (outside the scanner), and simultaneous EEG-MRI. The MRI scans included B_0 & B_1^+ mapping, GRE-based structurals, and resting-state fMRI at 1.6mm and at 0.8mm resolution (SMS-EPI).
MRI analysis: Several metrics of image quality and fMRI sensitivity were estimated for specific brain regions and networks: field heterogeneity and strength, spatial and temporal SNR, fractional amplitude of low-frequency fluctuations (fALFF) and intra-network consistency (INC) adapted from [4].
EEG analysis: The EEG data from EEG-fMRI runs were sequentially processed with gradient artifact (AAS + OBS), pulse artifact (K-means clustering), reference sensor-based and ICA-based artifact correction [2,5], and then compared to EEG recorded outside the scanner.

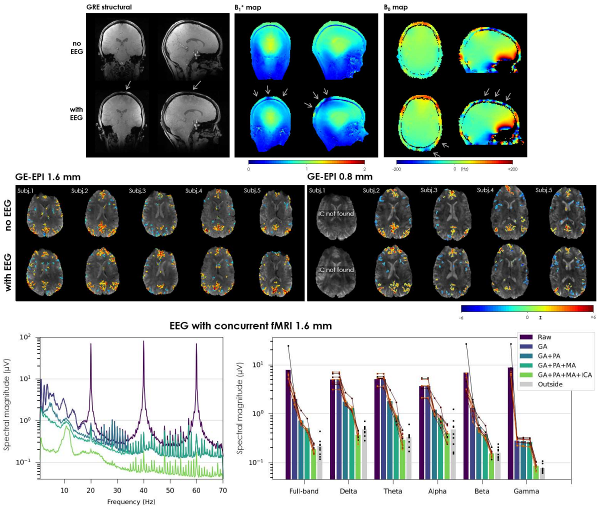

Figure 1: Impact of EEG on MRI quality (top) & default mode network detection (middle). Bottom: impact of MRI on EEG spectral profile across correction steps.

Results & discussion

No heating effects were detected on EEG electrodes or leads, and thus no safety issues. B_1 disruption was the main cause of MRI quality decrease when the EEG was in place (Figure 1-top), resulting in 11–17% loss in temporal SNR across the brain. No systematic losses in fALFF or INC were observed, and typical fMRI networks such as default mode could be found with and without EEG, in both fMRI resolutions (Figure 1-mid) – suggesting a low impact of EEG on fMRI sensitivity.
The EEG data recorded with concurrent fMRI showed important artifacts, but these were strongly reduced by the correction pipeline, uncovering the expected alpha peak and beta contributions typical of resting-state EEG; the corrected band power profile became comparable to that of EEG acquired outside MRI (Figure 1-bottom).

References

1. Jorge et al, Neuroimage, 105:132-144, 2015.
2. Jorge et al, Neuroimage, 120:143-153, 2015.
3. Meyer et al, J Neurosc Methods, 331:108518, 2020.
4. Korhonen et al, Network Neurosc, 1:254-274, 2017.
5. Jorge et al, Neuroimage, 191:21-35, 2019.

Acknowledgements

SNSF (grants 185909, 192749, 209470), CSEM, TIC-SITEM.

BENEFITS OF PIEZOELECTRIC MEASUREMENT TECHNOLOGY IN BIOMECHANICS AND LIFE SCIENCE

Foskien Bouman, Julian Hoch

Kistler Instrumente AG
Eulachstrasse 22, 8408 Winterthur

Introduction

Kistler has established a half-century legacy as a leading manufacturer of biomechanics measuring instruments, setting new standards. In universities, clinics, and rehabilitation centers, Kistler force plates are indispensable for research, sports performance diagnostics, motion analysis, clinical gait analysis, and occupational safety. Renowned for their durability and high precision, Kistler's piezoelectric sensors provide reliable measurement results even in the most demanding environments.

Piezoelectric Principle

The piezoelectric principle involves applying force to a piezoelectric crystal, causing a molecular-level charge shift within its lattice structure. This electric charge is collected on the crystal surface and converted into a voltage signal using a charge amplifier. A key advantage is the minimal deformation required, as the charge effect arises from shifts within the atomic structure. This allows for the creation of highly rigid structures with high natural frequencies, ideal for capturing rapid or high-frequency measurement events.

Benefits of Piezoelectric Force Plates

The key advantage of Kistler force plates lies in their use of rigid piezoelectric quartz crystal sensor elements, making them ideal for measuring dynamic forces. These sensors offer very high natural frequencies in both vertical and shear dimensions, excellent dynamic response, and a wide measurement range with high resolution. These benefits contribute to precise measurement results, even under challenging conditions.

In biomechanical tests, the forces often increase at quite a high rate. Therefore, a force plate with a high natural frequency is essential for obtaining accurate measurement results. A high natural frequency allows for a high maximum measurement frequency, which is crucial for precise measurements of highly dynamic movement sequences. Piezoelectric force plates, with their higher natural frequency, can measure more dynamic movements, providing more reliable values (e.g. for peak forces, rate of force development) compared to strain gauge force plates.

Additionally, a high natural frequency significantly benefits measurements of sports activities with low-frequency components. The greater the difference between the force plate's natural frequency and the movement's frequency content, the less likely the measurement frequency is overstated, thus minimizing errors.

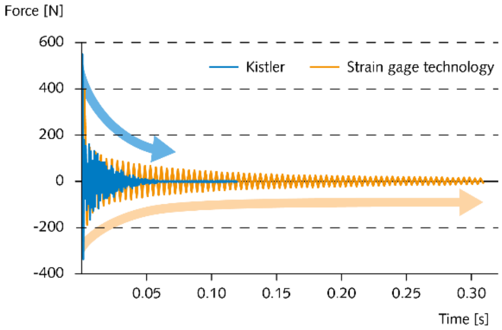

Figure 1: Dynamic response of piezoelectric sensors

Compared to piezoelectric sensors, strain gauge force plates must be selected for a specific measurement range and risk damage if this range is exceeded. When exposed to large forces, they will not generate signals of adequate quality when subjected to lower loads.

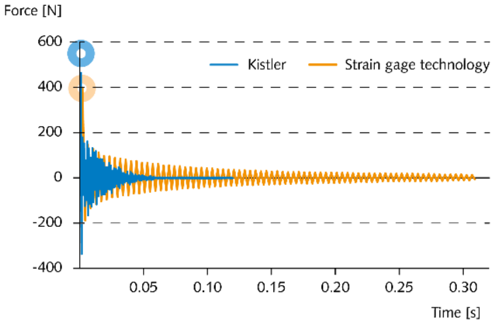

Figure 2: Peak force measurement

Moreover, Kistler force plates are exceptionally cost-efficient, showing no signs of fatigue even after millions of loading sequences and numerous temperature cycles. This durability ensures long-term reliability in withstanding overloads without damage, making them a robust choice for various measurement needs.

ABNORMAL CARDIAC RHYTHM DETECTION FROM PHOTOPLETHYSMOGRAPHY SIGNALS

Loïc Jeanningros* (1,2), Jérôme Van Zean (1), Mathieu Le Bloa (3), Cheryl Teres (3), Claudia Herrera Siklody (3), Alessandra Pia Porretta (3), Patrizio Pascale (3), Adrian Luca (3), Jorge Solana Muñoz (3), Giulia Domenichini (3), Théo A. Meister (4), Rodrigo Soria (4), Hildegard Tanner (4), Jean-Marc Vesin (2), Jean-Philippe Thiran (2), Etienne Pruvot (3) , Emrush Rexhaj (4), Mathieu Lemay (1) and Fabian Braun (1)

1. Swiss Center for Electronics and Microtechnology, Switzerland; 2. Swiss Federal Institute of Technology Lausanne, Switzerland; 3. Service of Cardiology, Lausanne University Hospital, Switzerland; 4. Department of Cardiology and Biomedical Research, University Hospital Bern, University of Bern, Switzerland

*Corresponding author: loic.jeanningros@csem.ch

Introduction

Cardiac arrhythmias (CA) are a critical health concern affecting a growing proportion of the population [1]. Wearable devices based on photoplethysmography (PPG), such as smartwatches, are gaining in popularity. They present significant benefits over traditional monitoring devices, being both convenient for everyday life monitoring and available prior to any medical visit. While PPG has already demonstrated high performance in detecting atrial fibrillation (AF), the most common CA, its efficacy in identifying and distinguishing other CAs remains uncertain.

In this study, we applied a PPG-based abnormal rhythm detection model to two datasets including five distinct types of pathological CA. The objectives were to evaluate the capability of model to detect various CAs as abnormal rhythms, and to delineate the limitations of abnormal rhythms detection using only inter-beat intervals (IBI).

Material and Methods

Datasets: The clinical dataset consists of recordings from 75 patients (172 h) referred for an electrophysiological procedure and includes five types of pathological CA in addition to normal sinus rhythm. The ambulatory dataset shows two pathological CAs (AF and bigeminy), acquired from 79 patients (5620 h) in free-living conditions.

Preprocessing: The onsets of PPG beats were identified using a beat detector that has demonstrated superior performance in the presence of CAs [3], to derive IBIs. IBIs were then segmented into 30-second windows. Windows with insufficient quality, heterogeneous cardiac rhythms, or motion artifacts were excluded from analysis.

Prediction: A pre-trained recurrent neural network processed IBI sequences to predict the likelihood of a window exhibiting an abnormal rhythm.

Post-processing: Windows were classified as normal, abnormal, or undecidable based on their likelihood. To validate a prediction, at least 3 out of 4 consecutive windows needed to have the same label; otherwise, they were categorized as undecidable.

Results

After window exclusion, 58 h (33.7%) of the clinical dataset and 2383 h (42.4%) of the ambulatory dataset were analyzed. Sinus rhythms were correctly identified as normal (99.3% and 97.6%). AF were well detected as abnormal (100% and 97.5%), in contrast to atrial flutter (52.5%) and ventricular tachycardia (43.8%).

Table 1: Abnormal rhythm detection performance.

Dataset	**Clinical**	**Ambulatory**
Accuracy	92.7%	97.6%
Sensitivity	79.7%	96.8%
Specificity	99.3%	97.6%
Undecidable proportion	7.0%	8.6%
Detailed rhythms		
Normal sinus rhythm	99.3%	97.6%
Atrial fibrillation	100.0%	97.5%
Bigeminy	100.0%	91.8%
Atrial flutter	52.5%	-
Atrial tachycardia	85.2%	-
Ventricular tachycardia	43.8%	-

Discussion

The abnormal cardiac rhythm detection model demonstrated satisfactory accuracy on the clinical dataset and high accuracy on the ambulatory dataset, particularly excelling in the detection of AF and bigeminy. However, it showed suboptimal performance for atrial flutter and ventricular tachycardia, likely due to the high regularity of IBIs in some episodes of these arrhythmias. These findings suggest that using IBIs alone limits the detection of certain arrhythmias. Further investigations into the spectral characteristics of the PPG signal and the morphology of individual PPG beats are necessary to enhance detection performance.

References

1. Krijthe et al, European Heart Journal, 34:2746-2751, 2013.
2. Pereira et al, npj Digital Medicine, 3:1-12, 2020.
3. Jeanningros et al, Physiological Measurement, 45:025005, 2024.

SSBE 2024: PYTHON-BASED OPEN SOFTWARE FOR EEG-BASED BRAIN-MACHINE INTERFACES

Omar Lone*, Manuel Weiss, Daniel Baumgartner, Ricardo Chavarriaga

1. ZHAW School of Engineering, Switzerland
*Corresponding author: lone@zhaw.ch

Introduction

The growing desire to seamlessly and intuitively interact with technology has driven significant advancements in two key areas, namely Brain-Machine Interfaces (BMIs) and Human-Machine Interfaces (HMIs). BMIs represent the establishment of a direct link between the brain and external devices. Translating thought into action by decoding brain activity captured with sensors like EEG, MEG or fMRI. HMIs, on the other hand, encompass a broader range of technologies that facilitate information exchange between humans and machines. The type of interaction ranges from conventional keyboards and mice to complex interfaces as advanced virtual reality systems with haptic feedback. As these fields continue to evolve, the convergence of human and machine intelligence has the potential to expand various scientific domains, including neurorehabilitation, prosthetic control, and communication for individuals with disabilities. Electroencephalography (EEG) holds promise for brain-computer interfaces (BCIs), but current setups limit real-world use. Traditional EEG requires controlled labs, and specialized software, hindering portability and ease of use. Existing software tools offer some solutions but fall short. GUI-based interfaces like OpenVibe, while offering closed-loop support, lack flexibility for integration. Conversely, powerful Python libraries like EEG-ExPy struggle with real-time processing needed for closed-loop experiments [1], [2], [3].

Material and Methods

This project presents a modular Python framework for real-time EEG processing, see Figure 1. Built on open-source tools, it offers data acquisition, pre-processing, feature extraction, classification, and real-time visualization, as illustrated in Figure 2. This facilitates the development and evaluation of processing strategies for BCI applications. It is user-friendly for programmers and data scientists, enables the usage of all commonly used Python modules, is configurable, and allows for an easier interdisciplinary workflow on BCI systems and provides benchmark for different acquisition methods, see Table 1.

Table 1: Acquisition Benchmark

API	Get Data Time per call [ms]
LSL	3.98
Unicorn C	3.97
Unicorn Python	3.88
BrainFlow	0.09

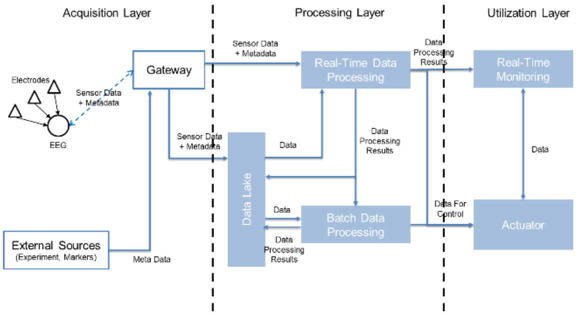

Figure 1: Illustration of the framework

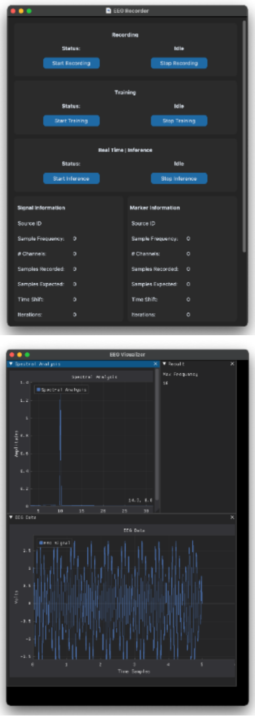

Status: Idle

Status: Idle

Status: Idle

Signal Information
Source ID
Sample Frequency: 0
Channels: 0
Samples Recorded: 0
Samples Expected: 0
Time Shift: 0
Iterations: 0

Marker Information
Source ID
Sample Frequency: 0
Channels: 0
Samples Recorded: 0
Samples Expected: 0
Time Shift: 0
Iterations: 0

Max Frequency
16

Figure 2: Signal Visualization

References

[1] R. K. Das, A. Martin, T. Zurales, D. Dowling, and A. Khan, “A Survey on EEG Data Analysis Software,” *Sci*, vol. 5, no. 2, Art. no. 2, Jun. 2023, doi: 10.3390/sci5020023.

[2] H. Anowar, “A Python-based Brain-Computer Interface Package for Neural Data Analysis”.

[3] M. A. Lebedev and M. A. L. Nicolelis, “Brain-Machine Interfaces: From Basic Science to Neuroprostheses and Neurorehabilitation,” *Physiol. Rev.*, vol. 97, no. 2, pp. 767–837, Apr. 2017, doi: 10.1152/physrev.00027.2016.

ASSOCIATIONS BETWEEN NOCTURNAL HYPOGLYCAEMIA AND CONSUMER-GRADE SENSOR DATA IN PEOPLE WITH DIABETES

C. Mendez Schneider (1,2), Asli Kaykayoglu (1), Livia Brun del Re (1), M. Rothenbühler (3), D. Hadorn (4), M. Laimer (1), L. Witthauer* (1)

1 Department of Diabetes, Endocrinology, Nutritional Medicine and Metabolism, Inselspital, Bern University Hospital, University of Bern, Bern, Switzerland; 2 Graduate School for Cellular and Biomedical Sciences, University of Bern, Bern, Switzerland; 3 Diabetes Center Berne, Bern, Switzerland;
4 QUMEA AG, Solothurn, Switzerland

**Corresponding author: lilian.witthauer@unibe.ch*

Introduction

Hypoglycaemia is a major cause of concern in the management of diabetes. More than half of all severe hypoglycaemic episodes occur during sleep. Continuous glucose monitoring devices (CGMs) have been shown to reduce the time spent in hypoglycaemia. However, they still have limitations, such as a short lifetime, limited reliability during low blood glucose levels, and invasiveness. Advances in sensor technologies allow for cost-effective, scalable, and non-invasive monitoring of changes in physiological and motion parameters in people with diabetes. Thus, using a radar sensor and consumer-grade smartwatches, we examined the relationship between nocturnal hypoglycaemia and physiological and motion parameters.

Material and Methods

In a pilot study, physiological data was gathered using two smartwatches (Garmin Venu 2 and Fitbit Sense 2) during sleep, while motion data was captured through a ceiling-mounted radar sensor (RADIQ1, Qumea). The data collection took place at the participant's homes over a study duration of 10 to 15 nights. The study includes adults with diabetes mellitus on insulin therapy, excluding participants with cardiac arrythmia, or any comorbidity or use of medications known to affect sleep patterns. In a preliminary analysis mixed-effects logistic regression models were employed. In both models, participants were treated as random effects. Radar data (N=13 participants, n=123 nights) was included as fixed effect in the first model, and smartwatch data (N=17 participants, n=135 nights) in the second model.

Results

The first model showed significant associations between radar data and nocturnal hypoglycaemia (Figure 1A). Likewise, the second model showed significant associations between heart rate variability (odds ratio = 0.49, 95% CI [0.41, 0.58], $p < 0.01$) and temperature (odds ratio = 0.85, 95% CI [0.81, 0.89], $p < 0.01$) on one side and nocturnal hypoglycaemia on the other side (Figure 1B).

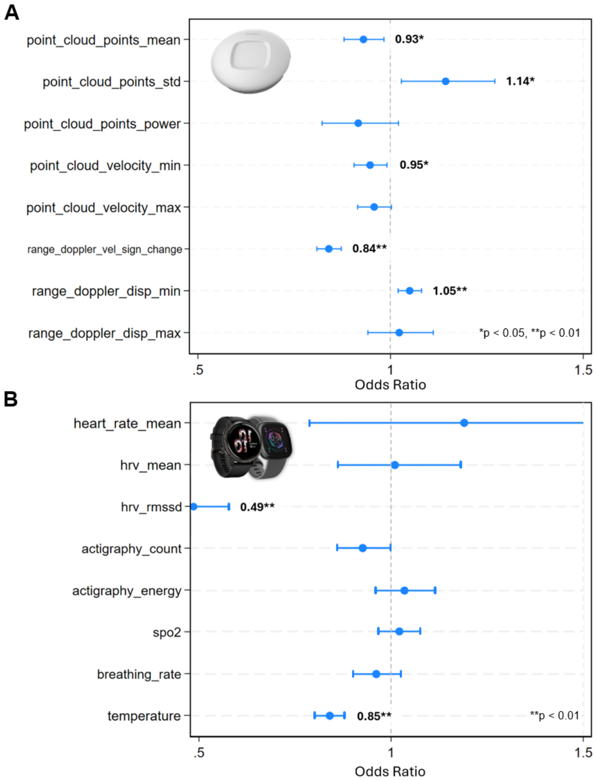

Figure 1: Forest plots of mixed effect logistic regression for radar (A) and smartwatch (B) data.

Discussion

Preliminary results suggest that data from a radar sensor and consumer-grade smartwatches can monitor motion and physiological parameters associated with nocturnal hypoglycaemia in people with diabetes. This data has the potential to enhance the accuracy of state-of-the-art CGMs and to be used for direct detection of nocturnal hypoglycaemic episodes.

Acknowledgements

This work was supported by the Diabetes Center Berne Foundation, Vontobel Foundation under application No. 0847/2022, and Innosuisse under funding application No. 62023.1 INNO-LS.

ADVANCES ON REAL TIME M/EEG NEURAL FEATURE EXTRACTION

Payam S. Shabestari (1), Delphine Ribes (2), Lara Défayes (2) and Patrick Neff* (1)

1. Department of Otorhinolaryngology, Head and Neck Surgery, University Hospital Zurich, Switzerland
2. EPFL+ECAL Lab, Ecole Polytechnique fédérale de Lausanne, Lausanne, Switzerland
**Corresponding author: patrick.neff@uzh.ch*

Introduction

Neurofeedback is a psychophysiological method where participants receive real-time feedback on their brain activity to help them self-regulate. This control over specific neural areas can lead to changes in behavior. As an early form of brain-machine interfaces (BCI), neurofeedback offers new insights into brain function and neuroplasticity [1]. It starts with observing neural activity, using methods like M/EEG, ECoG, fMRI, and fNIRS. Univariate approaches focus on signals from a single channel or region, such as an evoked potential. Common feedback methods include calculating power in a specific frequency band or measuring functional connectivity between two channels. This signal is then presented to the individual through visual, auditory, haptic, or electrical feedback, enabling the user to modify neural function. Shifting from spectral measures to signal complexity and graph analysis, as well as moving from sensor space to source space activation, could enhance neural targeting accuracy [2]. Our goal is to develop a sub-project within the broader MNE academic software package [3] whose goal is to implement and provide a set of algorithms allowing users to assemble complete data analysis pipelines that encompass most phases of M/EEG data processing. This sub-project namely as MNE-NF will include efficient algorithms from traditional to advanced ones compatible with different recording systems to extract neural targets from brain signals in real time. Our research aims to standardize the extraction of neural features from streamed M/EEG signals using both traditional and advanced methods, which could potentially enhance neurofeedback efficacy.

Material and Methods

The initial phase of our pipeline involves connecting to the data stream server to receive data with minimal latency, using a desired buffer size to track and refresh the data with new samples continuously. This allows us to view or access the latest samples within a specified window size, e.g. one second. This part is executed using the MNE-LSL Python package [4]. An optional baseline recording can be performed prior to main recording phase for more accurate source modeling or aperiodic component estimation of power spectral density of the individual. The next phase involves computing features from the accessed data. The implemented methods include *sensor/source powers*, *individual peak power* (i.e. the spectral power around the frequency with maximum activity), *band ratio*, *argmax freq* (i.e. the frequency with maximum activation), *entropy*, *spectral connectivity* in both sensor and source level, *cfc* (i.e. cross frequency coupling) and *graph connectivity* in both sensor and source levels, which is implemented via the method described in [5]. The schematic of the proposed pipeline is shown in Figure 1. To benchmark and assess the performance of the implemented methods, we simulated recordings by introducing artificial activation in a specific brain region(s) or spectral connection between two brain regions at specific time points. We then conducted a mock stream to evaluate the accuracy of these methods in tracking neural feature variation, as well as assessing the acquisition delay of the system and the delay of each method in computing the neural feature.

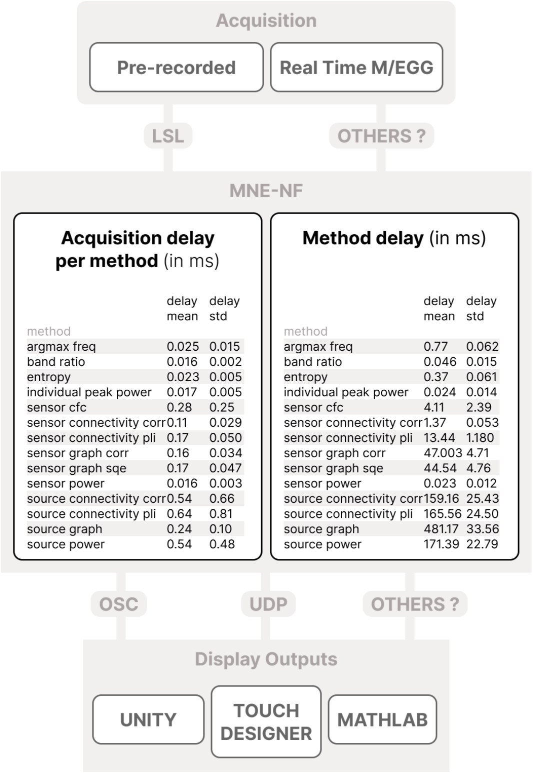

Acquisition delay per method (in ms)

method	delay mean	delay std
argmax freq	0.025	0.015
band ratio	0.016	0.002
entropy	0.023	0.005
individual peak power	0.017	0.005
sensor cfc	0.28	0.25
sensor connectivity corr	0.11	0.029
sensor connectivity pli	0.17	0.050
sensor graph corr	0.16	0.034
sensor graph sqe	0.17	0.047
sensor power	0.016	0.003
source connectivity corr	0.54	0.66
source connectivity pli	0.64	0.81
source graph	0.24	0.10
source power	0.54	0.48

Method delay (in ms)

method	delay mean	delay std
argmax freq	0.77	0.062
band ratio	0.046	0.015
entropy	0.37	0.061
individual peak power	0.024	0.014
sensor cfc	4.11	2.39
sensor connectivity corr	1.37	0.053
sensor connectivity pli	13.44	1.180
sensor graph corr	47.003	4.71
sensor graph sqe	44.54	4.76
sensor power	0.023	0.012
source connectivity corr	159.16	25.43
source connectivity pli	165.56	24.50
source graph	481.17	33.56
source power	171.39	22.79

Figure 1: An overview of MNE-NF pipeline starting with collecting data from streamed source to output display, along with acquisition and method delays for a sample recording with sampling frequency of 500 Hz.

References

1. Sitaram et al, Nature Reviews Neuroscience, 18.2 : 86-100, 2017.
2. White et al, Frontiers in behavioral neuroscience 8: 373, 2014
3. Gramfort, et al, Frontiers in neuroscience 7 : 70133, 2013
4. https://github.com/mne-tools/mne-lsl
5. Kalofolias, Vassilis, Artificial intelligence and statistics, 2016.

TOWARDS A ROBUST ELECTROMAGNETIC TRACKING SYSTEM FOR DEEP BRAIN STIMULATION SURGERY

Céline Vergne*(1,2,3), Morgan Madec (2), Raphael Guzman (3,4), Joris Pascal (1), Ethan Taub (4), Frédéric Bourgeois (1) and Simone Hemm (1)

1. *Institute for Medical Engineering and Medical Informatics, School of Life Sciences, University of Applied Sciences and Arts Northwestern Switzerland, Muttenz, Switzerland.*
2. *ICube laboratory, University of Strasbourg – CNRS, Strasbourg, France.*
3. *Department of Biomedical Engineering, Faculty of Medicine, University Basel, Allschwil, Switzerland.*
4. *Department of Neurosurgery, University Hospital Basel, Basel, Switzerland.*

*Corresponding author: celine.vergne@fhnw.ch

Introduction

Electromagnetic tracking (EMT) technique is highly effective for neuronavigation, offering real-time wireless guidance of tools without needing a line of sight. However, available EMT systems are inmcompatible with the standard surgical procedure for the placement of deep brain stimulation (DBS) electrodes with a stereotactic system [1]. This incompatibility arises from distortions induced by the stereotactic system within the tracking volume [2], significantly degrading tracking performance [3]. Most distortions result from the EMT system's alternating magnetic field, necessary for localizing the associated inductive sensors. To overcome this issue, we developed a new EMT system, ManaDBS, using on-chip magnetometers and quasi-static magnetic fields. This study compares the tracking performance degradation of ManaDBS to the commercial NDI Aurora® system in the presence of a stereotactic system.

Material and Methods

The two navigation systems, NDI Aurora® and ManaDBS, consist both of a magnetic field generator (FG) of 20 cm x 20 cm x 7 cm and a flexible tube of 1.4 mm diameter, integrating a magnetic sensor at the tip. Within a volume of 15 x 15 x 15 cm^3, similar to the head's volume, 100 positions were acquired with both EMT systems. The offset distance, defined as the distance between the FG and the closest point from the measurement volume (MV), was set at 18 cm. (Fig 1.A). Two settings were investigated: first, the Baseline setting, without any external electromagnetic perturbations and second, the Gframe setting, by positioning the stereotactic system (Leksell® Stereotactic G system, Elekta AB) around the MV. An optical tracking system was used as a reference. The position and orientation errors were calculated as the Euclidean distance between the positions and orientations obtained by the EMT system and the reference.

Results

This study revealed increased localization errors for the Aurora system when a stereotactic system was introduced, whereas the ManaDBS maintained consistent localization performance (1.57 mm position error and 1.01° orientation error for both settings). For the Aurora System, the position error increased from 0.66 mm (0.94 °) for the Baseline up to 2.34 mm (0.94°) with the Gframe (Fig 1.B).

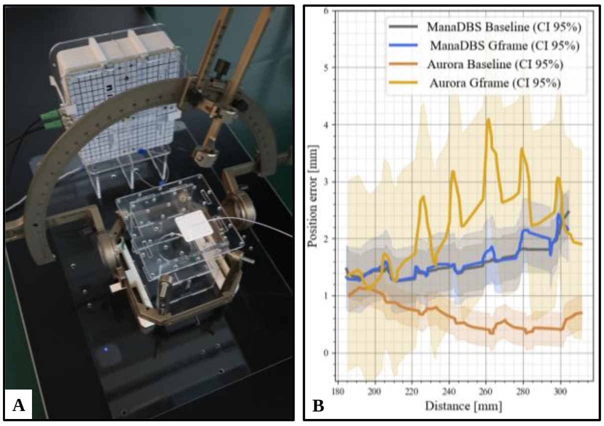

Figure 1: A) Picture of the Gframe setup including the Stereotactic G system (frame and arc) and the ManaDBS system. B) Position errors for the ManaDBS and the Aurora system as a function of the distance to the FG.

Conclusion

This study compares the performance of a commercial system and a novel EMT system currently under development. The results indicate that ManaDBS is compatible with the stereotactic system, gold standard technique of the DBS surgery.

References

1. Burchiel et al, Stereotactic and Functional Neurosurgery, 98:37–42, 2020.
2. Franz et al, IEEE Transactions on Medical Imaging, 33:1702–1725, 2014.
3. Nafis et al, Jr. Proceedings of the SPIE, 6141:152-167, 2006.

Acknowledgements

This research was funded by the Swiss National Science Foundation (SNSF) [204448].

VELOCITY BASED TRAINING: PREDICTION OF MAXIMAL STRENGTH

Basil Achermann* (1,2), Silvio Lorenzetti(1)

1.Institute of Data Analysis and Process Design, ZHAW, Winterthur, Switzerland;
2. Institute for Biomechanics, ETH, Zurich, Switzerland;

*Corresponding author: achr@zhaw.ch

Introduction

The quantification of one repetition maximum (1RM) is fundamental to resistance training program design. Questions arise about the accuracy of predicted 1RM values [1] and whether it is affected by variables such as gender or technical characteristics. Positive findings were reported but differences are expected between exercises and populations [2].

Material and Methods

For this study warm up sets at 20, 40, 60, 80 and 90 percent of the most recent 1RM (one-repetition maximum) were used to predict 1RM free weight back squat strength. The data from 28 healthy resistance-trained volunteers (16m,12w) were used for this study (173.7±8.6 m, 80.3±11.4 kg). All subjects were free from any musculoskeletal injuries, able to perform the full depth back squat and performed the same procedure twice. Velocity was recorded by a Gymaware linear position transducer; the velocity profile was captured with a barbell-mounted IMU sensor (Apple Watch 9). Every squat was performed to full depth with maximal concentric effort.

Results

The actual 1RM (138.1±32.5 kg) was stable between 2 sessions (ICC = 0.99; SEM =3.4kg; CV=3.9%; ES=-0.01). Predicted 1RM from 5 warm-up sets including 90% of 1RM were reliable (ICC = 0.94; SEM = 10.2 kg; CV = 9.7%; ES = 0.06) and valid (r =0.97; SEE= 17.4 kg; CV = 8.0%; ES = 0.35) of the predicted 1RM methods. A significant difference in the mean difference between true 1RM and predicted 1RM was found between genders. Specifically, males had a mean difference of 17.7 kg (95% CI [10.4, 25.0]), while females had a mean difference of 7.4 kg (95% CI [3.9, 11.0]); p = 0.01337. No significant difference was observed for the velocity profile. Bland-Altman plot was used to assess the agreement between 1RM and predicted 1RM for session 1. The mean difference was found to be 13.2 kg, with limits of agreement ranging from -9.6 to 35.9 kg. The plot revealed a trend of higher errors at higher mean values, indicating potential proportional bias. See Figure 1 for details.

Discussion

The load-velocity prediction of the free-weight back squat 1RM was found to be moderately reliable and valid but not accurate enough to predict maximal strength on a daily basis. The load-velocity relationship cannot accurately predict 1RM, especially at higher loads. Higher loads showed larger differences, with males exhibiting larger differences than females, indicating potential proportional bias. If this difference is caused by gender or by other factors such as trainings experience must be further evaluated. Furthermore, a successful 1RM backsquat test involves more than simply lifting heavier weights; it includes, but is not limited to, mental factors, technical level, core strength, strategic approaches, and barbell dynamics. While LVP assesses progress and daily readiness at submaximal weights, it may not effectively measure maximal strength at highest levels of performance.

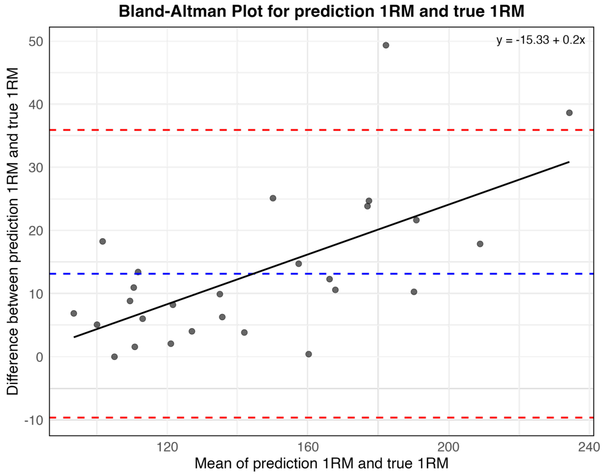

Figure 1: Bland-Altman plot showing the agreement between measured Max Load and Predicted 1RM for session 1. Units are in kg.

References

1. Banyard, H.G.; Nosaka, K.; Haff, G.G. Reliability and Validity of the Load–Velocity Relationship to Predict the 1RM Back Squat. Journal of Strength and Conditioning Research 2017, 31, 1897–1904, doi:10.1519/JSC.0000000000001657.
2. Sayers, M.G.L.; Schlaeppi, M.; Hitz, M.; Lorenzetti, S. The Impact of Test Loads on the Accuracy of 1RM Prediction Using the Load-Velocity Relationship. BMC Sports Sci Med Rehabil 2018, 10, 9, doi:10.1186/s13102-018-0099-z.

Acknowledgements

This work was supported by grant 200021_192289/1 from the Swiss National Foundation. The study was conducted in accordance with the Declaration of Helsinki, and approved by the Ethics Committee of Berne, Nr: 2018-00742.

MUSCULOSKELETAL MODELING OF THE SCOLIOTIC SPINE: SENSITIVITY OF JOINT CENTER POSITIONS

Philippe Bähler* (1,2), Salvatore Conticello (1,2), Philippe Büchler (2), Stefan Schmid (1,3)

1. Bern University of Applied Sciences School of Health Professions, Switzerland
2. University of Bern ARTORG Center for Biomedical Engineering Research, Switzerland
3. University of Basel, Faculty of Medicine, Switzerland
**Corresponding author: philippe.baehler@bfh.ch*

Introduction

Accurate musculoskeletal (MSK) modeling of the spine is crucial for assessing intervertebral loads in patients with adolescent idiopathic scoliosis (AIS). The position of the joint center is essential and affects the lever arms and results of kinematics and dynamics simulations. In MSK models the spinal joint centers are fixed despite the fact that it moves during motion. This study investigates the sensitivity of personalized MSK models for AIS patients by systematically altering the position of the joint center and analyzing the changes in joint angles derived from inverse kinematics (IK) simulations.

Material and Methods

Two personalized musculoskeletal models of patients with AIS, developed by Rauber et al. (J. Biomech, 2024), were used to quantify the sensitivity of IK simulation to a shift in the position of the joint center. These models were developed using biplanar radiographs and were driven by motion capture and ground reaction force data. The T8 vertebra is the apex in both patients examined in this study (PA01: female, Cobb angle: 45°, age: 15; PA02: female, Cobb angle: 21°, age: 12). Joint angles at the apex were monitored during the IK simulations. The coordinates of the joint center were systematically varied in steps of 4 mm along the X, Y, and Z axis in a 5x5x5 grid. IK simulations were performed using OpenSim v4.5, driven by marker data from a sit-to-stand exercise. MATLAB R2023b (MathWorks, Inc., Natick, MA, USA) was used to automate the simulation pipeline and perform statistical analyses.

Results

The root mean square error (RMSE) was calculated relative to the original position of the joint center for 125 different joint center positions for each patient. The differences in RMSE values are shown in Figure 1. The green color represents a small deviation, with respect to the reference joint position, while the red color indicates a large deviation from the original joint center, colored in black. The joint angle deviates up to 4.3° when standing up and up to 3.3° when sitting down for PA01. The maximum RMSE deviation for PA02 is 2.8° when standing up and 2.9° when sitting. The joint angles were analyzed in flexion and extension.

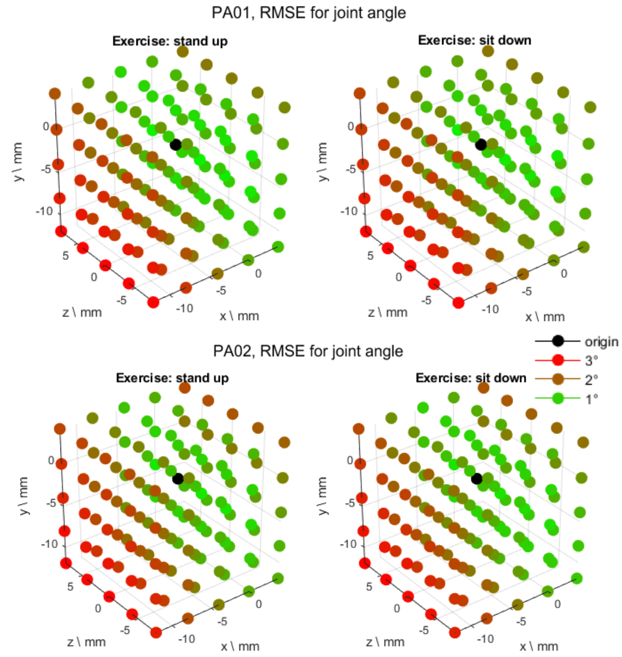

Figure 1: Visualization of RMSE between the original joint center and the shifted joint centers. Note the right-hand coordinate system used also by OpenSim.

Discussion

The root mean square error (RMSE) in joint angles between the original joint center and the shifted joint center reached up to 4.3°. The higher deviations can be seen in the patient with the more severe scoliosis. The shifts of the joint center position alter lever arms which affects the joint reaction forces. The range of center variation is comparable to other studies adjusting for the patient's endplate size. The z-direction variation is relatively large, especially during the sit-to-stand exercise, where no lateral movement is expected. The models used in this simulation do not take into account passive structures (e.g., ligaments, fascia), that contribute to limiting the spinal mobility and reduce the sensitivity of the joint center position. Further studies are needed to quantify this effect and to analyze the sensitivity at multiple joint levels for a higher number of patients.

Acknowledgements

We thank C. Rauber, L. Connolly, L. Poux, M. Schori, F. Galbusera, M. Deml and C. Hasler for previous work leading to this project. This work was supported by the Swiss National Science Foundation (SNSF; Grant-No.: 214986).

PRELIMINARY STUDY ON MEASURING BALANCE AND CONTROL IN THE ELDERLY USING AR AND VR TECHNOLOGIES

Andrea Kilchenmann* (1), Daniel Baumgartner (1), Michelle Haas (2), Bettina Sommer (2)

1. IMES Institute of Mechanical Systems, Zurich University of Applied Sciences, Switzerland
2. Institute of Physiotherapy, Zurich University of Applied Sciences, Switzerland
*Corresponding author: andrea.kilchenmann@zhaw.ch

Introduction

Falls are the leading cause of injuries in older adults, significantly reducing their quality of life [1]. Understanding the correlation between center of pressure (CoP) displacement and risk of fall highlights the importance of assessing dynamic balance [2]. Exergames are increasingly used today as a rehabilitation tool [3] and have great potential to improve motor balance and control reducing the risk of falling through targeted balance training [1].

This preliminary study aimed to compare older adults' subjective perception with objectively measured CoP across different conditions: a game played in augmented reality (AR), virtual reality (VR), and passthrough (PT) mode.

Material and Methods

Seven participants (4 male, 3 female) aged over 65 years (mean 71.43 ± 4.16) with no acute or chronic musculoskeletal or neurological diseases were recruited. The body mass index ranged from 18 to 28 kg/m^2.

Participants played a three-minute reaching game (grasping for fruits within arm's reach, Figure 1) with each technology in a randomized order to investigate the relationship between their preferred technology (from a questionnaire) and measured CoP (using a force plate) during reaching movements.

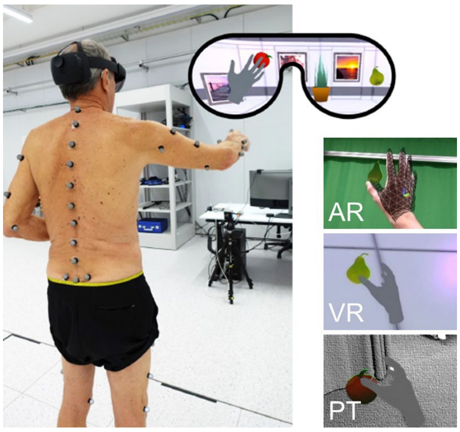

Figure 1: A participant playing the reaching game. The different tested modes (AR, VR, and PT) are shown on the right.

The trajectory of the CoP was reconstructed for each reaching movement (Figure 2) and the maximum deflection in the anterior-posterior (ΔCOP_x) and medial-lateral (ΔCOP_y) directions was calculated.

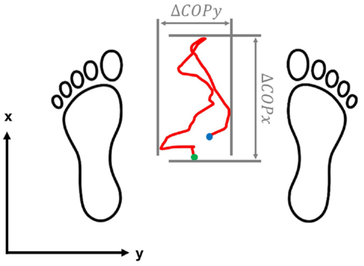

Figure 2: The trajectory of the CoP during one reaching movement (staring point in green, end point in blue).

Results

The results of the questionnaire suggest that the VR technology was subjectively preferred over AR and PT due to the good orientation in the room and the large field of view. Table 1 presents mean deflections across participants and technologies. Mean deflection of CoP in x-direction was 77.0 mm and y-direction 39.7 mm.

Table 1: Mean deflection of the CoP calculated for all reaching movements for the AR, VR, and PT mode.

	$\overline{\Delta COP_x}$ [mm]			$\overline{\Delta COP_y}$ [mm]		
	AR	VR	PT	AR	VR	PT
1	66	91	91	31	34	31
2	56	74	69	32	43	50
3	110	104	96	60	55	51
4	81	58	47	50	40	30
5	42	64	56	16	34	25
6	62	49	40	29	30	20
7	74	58	84	50	48	79
	70 ± 21	**71 ± 19**	**69 ± 22**	**38 ± 15**	**40 ± 9**	**41 ± 21**

Discussion

Subjective preference for VR did not result in reduced CoP deflection. Deflections were person-specific and did not notably differ between technologies. Further parameters such as e.g., total CoP path need to be considered which could express stability or instability criterion.

References

1. Delgado et al, Games Health J, 10(1):2-12, 2021.
2. Johansson et al, Hum Mov Sci, 66:117-123, 2019.
3. Ismail et al, Games Health J, 11(1):1-17, 2022.

Acknowledgements

This work was funded by the internal grant "Angewandte Gerontologie Age+" at ZHAW in 2023.

HOLOREACH: VR TRUNK CONTROL THERAPY - TOWARDS A USERFRIENDLY EXPERIENCE.

Marwen Mokni * (1), Christoph Bauer (1), Andrea Kilchenmann (2), Jens Bansi (3), Hadrien Gourdet (1), Owen Tanner (1), Jeremy Genter (2), Mandy Scheermesser (4), Daniel Baumgartner (2)
1. Therapy Science Lab, Lake Lucerne Institute, Switzerland; 2.Institute of Mechanical Systems, Zurich University of Applied Sciences, Switzerland; 3. Clinic Valens, Switzerland; 4. Institute of Physiotherapy, Zurich University of Applied Sciences, Switzerland, Switzerland
**Corresponding author: marwen.mokni@llui.org*

Introduction

Trunk control exercises are effective in improving trunk control, balance, and mobility after stroke.[1] Patients whose trunk control improves faster will be able to start earlier with gait and balance training.[2] Traditional trunk control rehabilitation is resource intensive regarding time and physical resources implying that the critical threshold for improvement might not be reached.[3,4,5].[6] Thus, further innovation is desirable to augment trunk control rehabilitation post stroke aiming at providing high dose trunk control training.[2,3,7,8] Mindful of this gap, we developed a prototype of an assisted therapy chair with a virtual reality application that produces exercise stimuli for trunk control training, in early post stroke.(Figure 1)[9,10] This device has shown good usability and effectiveness as an adjunct to conventional trunk control rehabilitation,[9–11] but better interactivity between patient, therapist and the application is required to facilitate engagement and adherence.[12] To achieve this, communication pathways between the patient, therapists, and game are developed and tested for their usability with 6 therapists to collect requirements for further development.

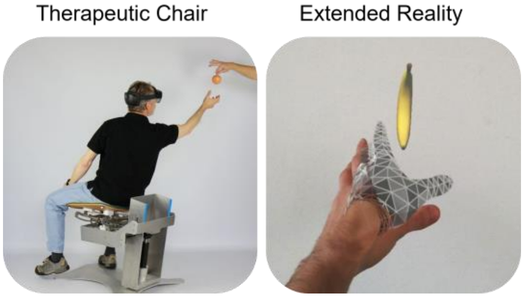

Figure 1: Holoreach

Material and Methods

The communication pathways for patient and therapist control consist of voice and icon communication pathways for the patient developed in Unity® and a tablet application for the therapist developed in Android®.(Figure 2) The patient and therapist can adapt parameters to change the difficulty of the exercise by adjusting exercise speed, duration, and cognitive demands. Through icon communication the patient can change in game parameters with buttons on a virtual table. Through voice communication the patient can use voice commands during the game to change the parameters. This allows to interact with the game (Pause and Play) and change the parameters without the need of any buttons. A tablet with a connection to the game enables therapists to adjust the parameters/difficulty of the game to ensure that the therapy session reaches the desired threshold of dosage. The tablet displays in game values like the score or countdown.

Figure 2: Communication Pathways

Results

Six therapists tested the pathways for 30 minutes each. Their feedback was collected using the thinking out loud technique and semi structured interviews. The therapists expressed an overall positive impression. Generally, the communication pathways are suitable for setting, controlling and adjusting the games difficulty. The therapists expressed suggestions for improvements, such as a broadcasting mode for the therapist to see the patients point of view of the game, and on the number, intuitiveness, and nature of the adjustable parameters, as well as general game settings.

Outlook

The improvements are presently being implemented and will be tested with patients and therapists for verification. The prototype contributes at various levels to the rapidly evolving advances in neurorehabilitation, particularly the practical aspect of exercise delivery.

References

1. Thijs et al, Cochrane Database Syst. Rev., 2023.
2. Saeys et al, Neural Repair, 26:231-238, 2012.
3. Veerbeek et al, PloS One, e87987, 2014..
4. Handerly et al, Stroke, 52:1768-1777, 2021.
5. Schwerz De Lucena et al, Sensors, 21:1502, 2021.
6. Mehrholz et al, Cochrane Database Syst. Rev, 2020.
7. Winters et al, NeuroRehabilitation, 43 :19-30, 2018.
8. Johansson et al, J. Neurol. 270:2890-2907, 2023.
9. Bauer et al, Appl. Ergon. 94 :103390, 2021.
10. Scheermesser et al, Nature Sci Rep, 14 :6598, 2024.
11. Thijs et al, J NeuroEngineering Rehabil, 18:120, 2021.
12. Loomis et al, Work, 76:1083-1098, 2023.

STATISTICAL SHAPE MODELLING IN SHOULDER MRI – AN APPROACH TO IDENTIFYING RISKS FOR ROTATOR CUFF TEAR PATHOLOGY

Martin E. Birchmeier* (1), Jeremy Genter (1), Eleonora Croci (2,3), Hanspeter Hess (4), Kate Gerber (4), Andreas M. Müller (3), Annegret Mündermann (2,3,5), Daniel Baumgartner (1)

1. Institute of Mechanical Systems (IMES), ZHAW; 2. Department of Biomedical Engineering, University of Basel; 3. Department of Orthopaedics and Traumatology, University Hospital Basel; 4. School for Biomedical and Precision Engineering, University of Bern; 5. Department of Clinical Research, University of Basel;

*birchma7@students.zhaw.ch

Introduction

Rotator cuff (RC) tear pathology significantly impairs shoulder function and is challenging to diagnose due to the complex and varying anatomy of the shoulder [1,2]. In this work, magnetic resonance imaging (MRI) and statistical shape modelling (SSM) were used to investigate anatomical variations of the scapula and humerus that correlate with RC tear pathology.

Material and methods

This work is a retrospective analysis of 43 participants who underwent MRI scans (n = 90, T1 VIBE DIXON) [3] to assess both of their shoulders, which were categorized into healthy (n=24), asymptomatic (n=24) and symptomatic (n=42) RC conditions based on the criteria established during recruitment. Principal component analysis (PCA) [4] was applied to 3D meshes [5] of the scapulae and humeri to identify principal components (PCs) indicative of significant anatomical variations.

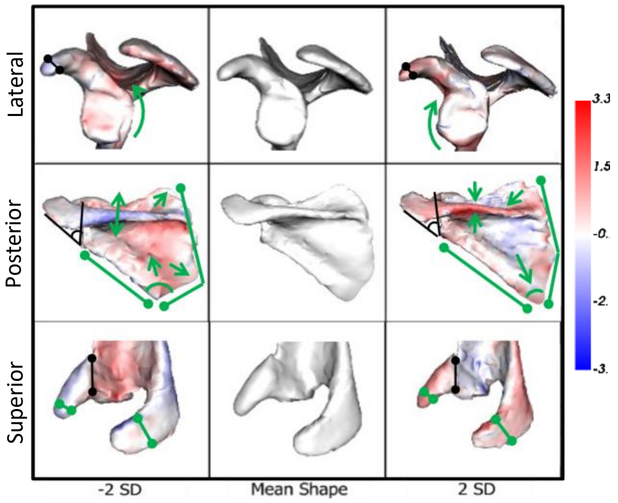

Figure 1: Example of the influence of PC7 on the mean scapula. Green: differences that can be observed, Black: significant differences of morphological measurements; Scale in cm.

Results

The PCA identified several PCs that differentiated between healthy, asymptomatic, and symptomatic RC conditions. In particular, PCs such as PC7 (see Figure 1), PC10 and PC12 of the scapula showed significant shape variances in the context of the pathology, indicating that the PC scores vary among the healthy, asymptomatic, and symptomatic shoulders. In symptomatic shoulders, PC7 and PC10 showed a pronounced anterior curvature, which refers to a forward bending of the glenoid surface. Also, PC7 and PC10 showed a posterior tilting of the glenoid. PC12 showed a wider lateral and medial border and changes in the coracoid and acromion lateral angle.

Discussion

The identified PCs highlight specific anatomical variations in the shoulder complex that are associated with RC pathology. For example, the increased anterior curvature and posterior tilting of the glenoid in symptomatic shoulders could affect shoulder biomechanics by altering the orientation of the muscle force line of action and their attachment angles and the articular interface with the humerus. These variations may increase shear forces in the joint, which have been associated with RC tears [6]. The wider scapula borders and altered acromion angles could affect the lever arm of the inserting muscles, increase force transmission in the shoulder joint, and hence increase the susceptibility to injury. These findings highlight the effectiveness of integrating SSM with MRI data to analyse and quantify the complex anatomical variations of the shoulder joint that may predispose individuals to RC pathology. The identified PCs allow further insight into the biomechanical implications associated with RC pathology. The presented approach may be a useful tool for aiding the diagnosis or even assist in predicting the risk for RC pathology. Future research should expand these analyses in a larger cohort and investigate the predictive value of the identified variations in the development of RC injury and pathology.

References

1. Zhao J et al. Clin Orthop Relat Res., 480(1):96–105, 2022
2. Yamaguchi K et al, J Bone Joint Surg Am, 1699–704, 2006
3. Croci E et al, JMIR Res Protoc. 11(12):e43769, 2022
4. Cates J et al, Elsevier, 257–298 p., 2017
5. Hess H et al, Diagnostics (Basel), 13(10):1668, 2023
6. Nyffeler RW et al, J Bone Joint Surg Am., 88(4):800–5, 2006

Funding

This project was funded by the Swiss National Science Foundation (SNF 320030_189082).

TESTING SCAPULOTHORACIC ELLIPSOID JOINT IMPLEMENTATIONS USING KINEMATICS FROM BIPLANAR FLUOROSCOPY

Eva Herbst(1,2), Stephen J. Ferguson(1), Philipp Moroder(2)

1. ETH Zürich, Switzerland; 2. Schulthess Klinik, Switzerland
*Corresponding author: eva.herbst@hest.ethz.ch

Introduction

In shoulder models, scapular motion is often constrained to the surface of an ellipsoid representing the thorax. This constraint stabilizes simulations and improves muscle activity estimates, and has been implemented as either 1-2 point constraints or via a scapulothoracic (ST) ellipsoid joint [1]. Here, we focus on this ST joint, which consists of 4 degrees of freedom (scapular elevation, abduction, upward rotation, and winging). Scapular movements can be affected by the ellipsoid definition [2]. The goal of this study was to develop and compare different methods of defining the ellipsoid joint.

Material and Methods

We implemented the ST ellipsoid from OpenSim [1] in ArtiSynth (www.artisynth.org). We used a biplane fluoroscopy dataset [3] of 20 healthy individuals performing coronal abduction (CA), scapular abduction (SA), and arm forward elevation (FE). We tracked 5 scapular markers with the ellipsoid models (glenoid center “GC”, trigonum spinae “TS”, inferior angle “IA”, posterolateral acromion “PLA”, and acromion “AC”). On one individual during CA, we tested: 1) a “dynamic ellipsoid” defined by IA and scapular contact point motion through time, as well as the jugular notch, and 1) a “static ellipsoid” based on 9 scapular markers in the resting position. The scapular contact point on the ellipsoid was the midpoint of AC, TS, and IA projected to the scapular surface. We tested 3 scapular joint frames: 1) “ISB Frame”: formed by rotating the International Society of Biomechanics scapular frame -90 degrees about Y; 2) “Plane” Frame: Frame 1 adjusted by aligning the Z axis to the normal vector of a plane fit to TS, AI, marker on the lateral scapular blade, and 3) “Initial Pos” Frame: Frame 1 adjusted to align the Z axis to the normal vector of a plane tangent to the ellipsoid at the scapular contact point, capturing the initial patient pose. The ellipsoid model with the lowest RMSE was tested on all other subjects. To test how well the “dynamic ellipsoid” tracks new motion, we used the ellipsoid based on CA motion to track FE motion.

Results

In the dynamic ellipsoid, the lowest root mean square tracking error (RMSE) was in the “dynamic ellipsoid” with the “initial pos” frame, followed by the “static ellipsoid” with the “initial pos” frame (Fig 1). Other individuals and motions are shown in Table 1.

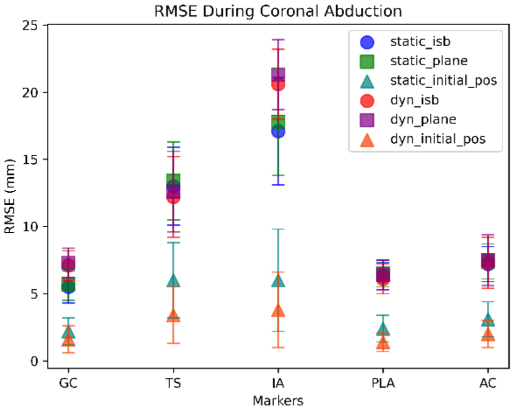

Figure 1: RMSE for markers in individual 1 during CA.

Table 1: Mean marker RMSE in mm for 20 subjects using “dynamic ellipsoid” with “initial pos” frame. Standard deviation in parentheses.

	GC	TS	IA	PLA	AC
CA	2.2 (0.8)	5.0 (2.4)	5.7 (2.2)	2.4 (1.2)	2.4 (0.9)
FE	2.5 (0.9)	6.0 (2.3)	6.3 (2.8)	2.9 (1.2)	2.8 (0.9)
SA	2.9 (1.3)	5.5 (2.0)	8.3 (2.9)	2.9 (1.2)	2.7 (0.8)
FE with CA Ellips.	3.8 (1.8)	8.2 (3.7)	8.6 (4.7)	4.0 (1.8)	3.5 (1.3)

Discussion

The “dynamic” ellipsoid with the “initial pos” frame performed best in individual 1 CA, and showed similar RMSE in all other individuals in CA, FE, and SA. However, the “dynamic” ellipsoid is closely fitted to the kinematics of one motion. Simulations often aim to investigate effects of interventions (e.g. implants, muscle activation) on motion. Here, we found that error increases when using an ellipsoid fit to one motion for tracking a new motion, but only slightly. Future work will focus on developing ST joints that permit new but physiologically plausible motions, as well as testing additional contact points and winging axes.

References

1. Seth et al. PLOS ONE 11(1): e0141028, 2016
2. Blache et al. Med. & Bio. Eng. & Comp. 60(7): 2065, 2022
3. Henninger. Dataset: doi.org/10.5281/zenodo.10972005, 2024.

ESTIMATION OF THE PREOPERATIVE VARIABLES EFFECT ON POSTOPERATIVE TOTAL SHOULDER ARTHROPLASTY COMPLICATIONS

Pezhman Eghbali (1), Osman Berk Satir (2), Fabio Becce (3), Patrick Goetti (3),
Philippe Büchler (2), Dominique Pioletti (1), Alexandre Terrier (1,3)

1) Ecole Polytechnique Fédérale de Lausanne (EPFL), Switzerland, 2) ARTORG Center for Biomedical Engineering Research, Switzerland, 3) Lausanne University Hospital (CHUV), Switzerland

**Corresponding author: pezhman.eghbalishamsabadi@epfl.ch*

Introduction

Total shoulder arthroplasty (TSA) for treating glenohumeral osteoarthritis (OA) with B2-B3 glenoids is particularly challenging due to the high rate of postoperative complications, such as loosening [1]. Different factors might be considered as causes of the complications. In this study our objective was to evaluate the causal effect of sex, age, and glenoid orientation on complications.

Materials and Methods

This retrospective study included 60 patients from our institutional TSA database who had primary OA and type B2-B3 glenoids. Patient characteristics, preoperative shoulder CT scans (glenoid version and inclination), and surgical techniques (including implant type and methods for compensating posterior wear) were recorded. Outcomes at the 2-year follow-up were evaluated using the Aldinger complications scale (ranging from 0 to 3) [2]. Of the 60 patients, 13 (21.67%) experienced complications, with 8 (13.3%) classified as Aldinger I and 5 (8.3%) as Aldinger III. We considered a binary outcome: major complications; no (no complication and Aldinger I), and yes (Aldinger III).

We considered a causal model, represented as a directed acyclic graph (Fig. 1). We evaluated the identifiability of the effect of each exposure on the outcome by do calculus and found the minimal adjustment set. We used Bayesian statistics for estimation of the effects

$$Y_i|C_i = 1 \sim Exponential(\lambda_i)$$
$$Y_i|C_i = 0 \sim Exponential - CCDF(\lambda_i)$$
$$\lambda_i = 1.0/\mu_i$$
$$log(\mu_i) = \alpha_{sex[i]} + \beta^{age}_{sex[i]} * age + \beta^{BMI}_{sex[i]} * BMI + \beta^{GVA}_{sex[i]} * GVA + \beta^{GIA}_{sex[i]} * GIA$$
$$\alpha, \beta \sim Normal(0, 1)$$

λ is the complication rate, μ is the time to complication, α is the average sex effect, and $\boldsymbol{\beta}$ are the age, BMI, GVA and GIA effects on the log of time to complication.

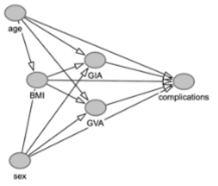

Fig. 1: *Directed acyclic graph (DAG) for describing the relationships between analyzed variables.*

Results

Male had a higher major complications rate, with an average of 29%, 10 years after surgery, while it was 22% for female at 70 years old. Aging decreased the major complications rate for females and males. Increasing age from 50 to 80 decreased major complications rate by 32% for females and 25% for males. Higher BMI decreased the major complications rate. Increasing BMI from 17 to 37 decreased major complications rate by 17% for females and 16% for males. The effect of glenoid version and inclination on major complications were small and had a huge uncertainty. Increasing GVA from -20 to 0 decreased major complications rate by 4% for females and 6% for males. Increasing GIA from -10 to 10 decreased major complications rate by 6% for females and 10% for males (Fig. 2).

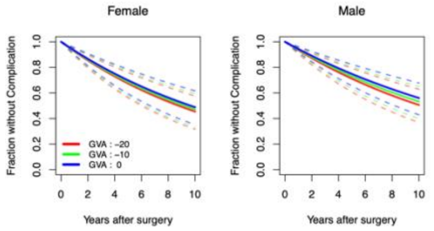

Fig. 2: *Survival curves (1-complications rate) (solid lines) and 89% compatibility interval (dashed lines) for female, male, and 3 values of GVA.*

Discussion

It has been reported that older patients have lower risk of revision after reversed total shoulder arthroplasty which was in accordance with our findings [3]. BMI is reported to not be a risk factor for mechanical surgical complications after TSA, which differed from our findings [4]. We found a negligible effect of glenoid version and inclination on major complications rate.

However, our foundlings were affected by low number of cases in this study. We recommend an extension of this study with a higher number of subjects.

References

1. B. Sharareh et al, JSES, 32:653-661, 2023.
2. P. R. Aldinger et al, Int Orthop. 34:517-524, 2010.
3. O. A Anakwenze et al, Perm J. 21:16-056, 2017.
4. C. G. Cogan et al, JSES, 32:253-259, 2022.

Acknowledgements

This work is supported by the Swiss National Science Foundation (Grant no: 189972).

A NEW MATERIAL MODEL FOR POLYCARBONATE URETHANE PCU

Daniel Baumgartner*, Roger von Mentlen, Mathias Huber, Robert Eberlein

Institute of Mechanical Systems (IMES), Zurich University of Applied Sciences ZHAW
**baud@zhaw.ch*

Introduction

Polycarbonate-Urethanes (PCU) represents a potential material for the use in artificial joint replacement in case of hemiarthroplasty. It has been shown that a soft mechanobiologic load transfer may be beneficial for retaining the native cartilage as articulating partner even better [1]. Additionally, good sliding properties were identified as an articulating material [2].
Although several experimental tests have been performed, time-depenent material models for the development of prosthesis designs are only partially available.
The aim was therefore to define and validate a FE material model for the simulation of PCU, based on mechanical, time-dependent material test parameters.

Material and methods

1. Used Material
Bionate® PCU with shore hardness 75D have been used (DSM, Germany) and moulded (Samaplast AG, Switzerland) in the shape of tension rods (ISO 527-2 Type 1A) for the mechanical tests. Same material has been applied for a ball-on-socket hip joint, applying a 1.5 mm thick PCU-layer on a CoCrMo-ball(Ø 32mm, Mathys AG).

2. Experimental tests
A confined compression-tension test and droptower test have been performed in the lab to derive basic parameters for the FE model. The droptower test applied different speed for pressure &tension.

3. Modelling
A «Three-Network-Viscoplastic (TNV), time-dependent Model has been used for defining the material model. The model calibration has been performed with the software MCalibration (Ansys Inc.)

4. Validation tests at hip ball-on-socket-joint
For the validation tests, 0.3mm compression has been applied on the ball-on-socket joint. Counterpart of the PCU-layered ball was the socket of a ceramic cup (Selesys, Mathys, Switzerland). The deformation properties were analysed by the experiment (n=3) and by FE model and compared by appling a time-dependent loading.

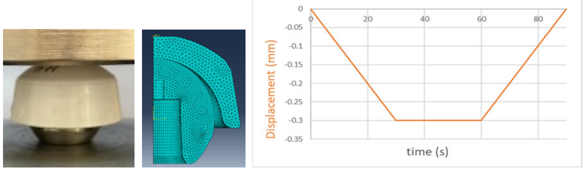

Fig. 1: Experimental setup using a ball-on-socket hip joint (left experiment, middle FEM-Model) and loading curve (right).

Results

1 Experimental tests

A compressive module of 2'200 MPa has been measured in the confined compression test. Together with the Young's Modulus of 210 MPa, a Poisson's ratio of 0.485 was calculated and integrated in the FE model.

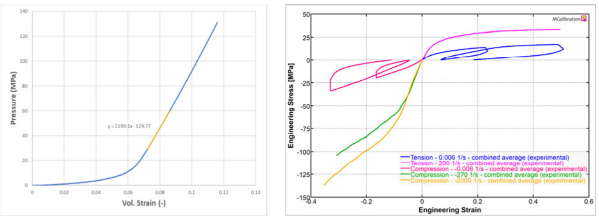

Fig. 2: Mean values of n=3 experimental tests for confined compression (left) and drop tower experiments at different speed (right): quasistatic tests for tension (blue) and compression (red) and at higher speed rates for compression (green/orange) and tension (magenta).

2 Validation Tests tests at hip ball-on-socket-joint

At a displacement of 0.3 mm, a loading of 8000N is applied which has been confirmed by the FE material model (10% lower max.) for the ball-on-socket joint.

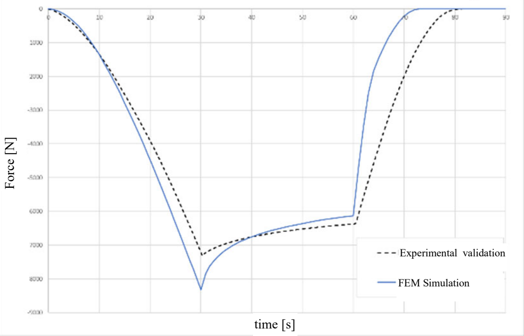

Fig. 3: Mean curves of n=3 experiments: Compressive response (dashed, black curve) vs. FE model (drawn curve).

Discussion

The FE-material model based on the basic mechanical tests has been confirmed in a validation setting by using ball-on-socket geometry (similar curve characteristics but 10% difference in the max. force values). The validated material model could be used for further prosthesis developments; saving experimental iteration steps.

References

[1] Luo Y, McCann L , Ingham E, Jin Z-M, Ge S and Fisher J. Polyurethane as a potential knee hemiarthroplasty biomaterial: an invitro simulation of its tribological performance, Proc. IMechE, Part H: J. Engineering in Medicine, 2010, 224: 415-25

[2] Sague J, Andreatta B, Egli R, Luginbuehl R. Low friction viscoelastic polymers as future materials for articulation with native cartilage tissue, CORS 2013, Venice, Poster P11.32

SILICON NITRIDE-BASED SCAFFOLDS FOR SPINAL FUSION WITH SOFT, SEMI-RIGID, AND HARD PROPERTIES

Xiaoyu Du* (1), Gurdial Blugan (2), Stephen Ferguson (1)

1. Institute for Biomechanics, ETH Zurich, Switzerland; 2. Laboratory for High Performance Ceramics, Empa, Swiss Federal Laboratories for Materials Science and Technology, Switzerland

*Corresponding author: xiaoyu.du@hest.ethz.ch

Introduction

A significant portion of the population suffers from spinal disorders such as intervertebral disc degeneration, disc herniation, spinal stenosis, and facet arthritis. Additionally, 10% to 20% of lumbar cases and up to 30% of cervical cases require surgical intervention. While spinal fusion surgery has high success rates, it also has high complication rates (10-30% in top hospitals) due to implant design and properties. Currently, implants that accurately mimic vertebral bone properties are lacking. Silicon nitride bioceramic (SiN) is promising for its high strength, osteogenesis, and antibacterial properties.

In our project, we developed silicon nitride-based scaffolds with different mechanical properties, ranging from soft to hard (i.e., porous SiN, PEEK/SiN, Hydrogel/SiN), and comprehensively assessed them for biomimetic mechanical properties, dynamic response, and cellular interactions to identify the best candidate for fusion scaffolds.

Material and Methods

Silicon nitride powder with a trimodal distribution and an average size of 0.8 ± 1.0 µm was supplied by SINTX Technologies Inc. (Salt Lake City, USA). The porous SiN was sintered with a foaming agent. SiN/PEEK with a triply periodic minimal surface (TPMS) structure was 3D printed using fused deposition modeling. Hydrogel/SiN, specifically SA-SiN/PVA, was prepared by casting polyvinyl alcohol/sodium alginate with silicon nitride via freeze-drying and chemical crosslinking. The detailed manufacturing processes are published in references [1-3].

Comprehensive mechanical and dynamic loading tests were performed on these scaffolds using an Instron dynamic testing machine, a drop tower, and a vibration setup. The cellular response of the scaffolds was evaluated using mouse pre-osteoblasts (MC3T3-E1).

Results

The Young's modulus of porous SiN with 70% porosity was 14.84 ± 0.91 GPa, and the compressive strength was 100.35 ± 3.39 MPa. Subsequent experiments revealed that porous SiN exhibited very limited energy dissipation compared to natural spinal tissues. In contrast, the Hydrogel/SiN scaffold demonstrated excellent energy absorption and rapid elastic recovery under quasi-static and impact loading scenarios. However, the elastic modulus of the Hydrogel/SiN scaffold is 1.20 ± 0.07 MPa, significantly lower than that of vertebrae. The PEEK/SiN scaffold with 30% porosity exhibited a compressive strength of 34.56 ± 1.91 MPa and an elastic modulus of 734 ± 64 MPa, similar to those of trabecular bone. Biological data revealed that incorporating silicon nitride stimulated osteogenic differentiation in both the PEEK/SiN and Hydrogel/SiN scaffolds.

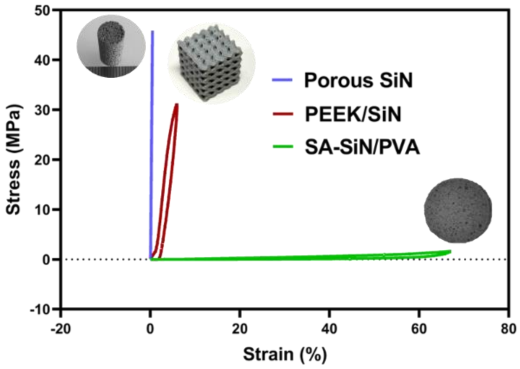

Figure 1: Stress-strain curve of the three types of SiN based scaffolds

Discussion

The porous SiN samples showed sufficient strength for load-bearing applications but still had much higher stiffness than trabecular bone and lacked damping properties. Conversely, the Hydrogel/SiN scaffold possesses great damping properties, which are crucial for preventing bone fractures, but they are not suitable as standalone load-bearing scaffolds. The PEEK/SiN scaffold showed the most promising mechanical properties, being very similar to natural vertebrae. Biological tests also confirmed its biocompatibility and osteogenesis potential. Consequently, based on the findings from our study, it can be inferred that PEEK/SiN scaffolds represent a promising avenue for future clinical applications as spinal implants and in the broader field of bone tissue engineering.

References

1. X.Y. Du et al., Ceram Int, 47(23):33525-33536, 2021.
2. X.Y. Du et al., Acs Appl Bio Mater 6(8):3319-3329, 2023.
3. X.Y. Du et al., J Mech Behav Biomed, 155, 2024.

Acknowledgements

This project has received funding from the EU Marie Sklodowska-Curie grant (No 812765).

SYNTHESIS AND STRUCTURAL CHARACTERIZATION OF BIOCOMPATIBLE GOLD NANOPARTICLES DISPERSED IN FATTY ACID

Mahsa Nasehi[1], Oya Tagit[2], Lilian Witthauer*[1]

1. Department of Diabetes, Endocrinology, Nutritional Medicine and Metabolism, Inselspital

2. Institute of Chemistry and Bioanalytics, School of Life Sciences, University of Applied Sciences and Arts Northwestern Switzerland, Muttenz, Switzerland

*Corresponding author: Lilian.Witthauer@unibe.ch

Introduction

Plasmonic nanoparticles (PNPs), especially those composed of noble metals, stand out among nanomaterials due to their unique localized surface plasmon resonance (LSPR). This phenomenon results from the confinement of photons within small particles [1].

Among PNPs, gold nanoparticles (AuNPs) are particularly prominent in biomedical sensing due to their photophysical properties, biocompatibility, functionalization potential, and chemical stability [2]. However, synthesizing AuNPs poses some challenges, such as the reliance on toxic synthesis pathways and their propensity to agglomerate in liquid environments. These challenges can be addressed by adjusting the synthesis components and applying appropriate coating layers to prevent aggregation and ensure non-toxicity [3].

Material and Methods

Synthesis of ALA- AUNPs

AuNPs were synthesized using a rapid and biocompatible method, described in reference [4]. The process involved mixing a reducing agent consisting of 10 mL of propylene glycol (PG) 2000 and 10 mL of alpha-linolenic acid (ALA, $C_{18}H_{30}O_2$) with a reaction mixture containing 1 mM $HAuCl_4.3H_2O$ and 1 mL of ALA. The obtained mixture was kept at 90°C for 15 min. As a result, the supernatant ultimately contained the AuNPs in ALA (ALA- AuNPs). The formation of ALA-AuNPs was initially confirmed by a color change from yellow to pink, as shown in Figure 1.

Figure 1: Visual representation of ALA-AuNPs sample.

Result and discussion

Figure 2 illustrates the dynamic light scattering (DLS) analysis of ALA- AuNPs, confirming their polydisperse nature with a polydispersity index of 1.7 %. The analysis indicates an average diameter of 100 ± 20 nm, inclusive of the coating layer. Figure 3 depicts the transmission electron microscope (TEM) image of ALA-AuNPs, revealing the average particles have a diameter of 70 nm. These findings suggest the presence of multiple layers of ALA surrounding the AuNPs.

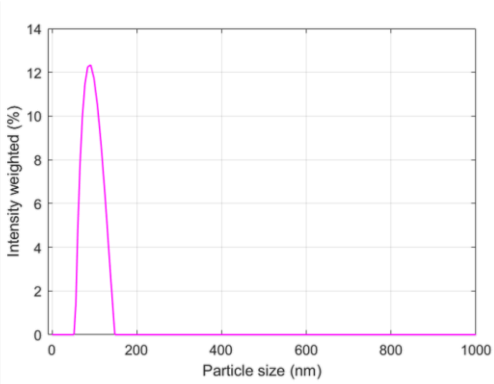

Figure 2: DLS measurement of ALA-AuPs

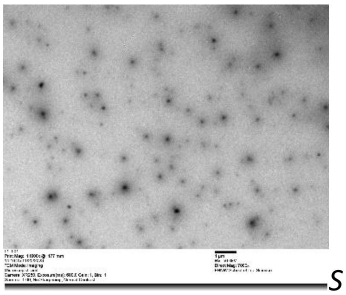

Figure 3: Transmission electron microscope image of ALA- AuNPs.

References

1. Sui M, Kunwar S, Pandey P, Lee J, Sci Rep, 9:1, 201
2. Botteon CEA, Silva LB, Ccana-Ccapatinta GV, Silva TS, Ambrosio SR, Veneziani RCS, et al, Sci Rep, 11:1, 2021
3. Sadrolhosseini AR, Abdul Rashid S, Zakaria A, J Nanomater, 2017:2017
4. Ghanavi J, Mostafavi M, Ghanavi Z, Method for the synthesis of metallic nano products, 2016.

THE ROLE OF WATER, LOADING RATE, AND TEMPERATURE ON THE MECHANICAL PROPERTIES OF LAMELLAR BONE

Jakob Schwiedrzik* (1), Cinzia Peruzzi (1), Christian Minnert (1), Tatiana Kochetkova (1), Jérémie Bérard (1), Christopher Dreimol (2), Ingo Burgert (2), Stefan Remund (3), Beat Neuenschwander (3), Johann Michler (1)

1. Laboratory for Mechanics of Materials and Nanostructures, Empa, Switzerland; 2. Institute for Building Materials, ETH Zurich, Switzerland; 3. Institute for Applied Laser, Photonics and Surface technologies (ALPS), Bern University of Applied Sciences, Switzerland

*Corresponding author: *Jakob.Schwiedrzik@empa.ch*

Introduction

Bone is a hierarchically structured composite material, the basic building blocks are type I collagen, mineral carbonated hydroxyapatite and water [1]. In addition, there is a small amount of non-collagenous proteins and proteoglycans. Water can either be classified as bound or free, where free water occupies the various pores [2]. Bound water, which is located at the interface between collagen fibrils and mineral crystals, has a major influence on load transfer by facilitating interface sliding and, thus, reducing shear stresses. This has a considerable effect on the mechanical properties, although the influence of different moisture levels on the mechanical properties has not yet been fully clarified. For this reason, micro pillar compression experiments were carried out to investigate the role of water, loading rate and temperature on the mechanical properties of lamellar bone.

Material and Methods

Micro-pillars were prepared by femtosecond laser ablation in ovine cortical bone with axial and transverse mineralized collagen fibril orientations and compressed at varying temperatures (25-60 °C), strain rates (0.1 to 100 1/s) and hydration states (mass gain between 3.1 to 8.3 wt. %). Finite element simulations were carried out in order to correct for the taper of the ablated micro-pillars. Raman spectroscopy was used to determine the mineral-to-matrix ratio, the collagen quality and the orientation of the mineralized collagen fibrils. Finally, a linear fitting approach was applied to isolate the effect of humidity and temperature on the yield stress.

Results

The predominant deformation and fracture mechanisms depend strongly on the fibril orientation towards the loading direction as illustrated in the post-mortem SEM images (Figure 1). The yield strength is therefore significantly lower compared to the axial direction. These findings are supported by a major difference in average activation volumes of 0.25 nm^3 and 0.64 nm^3 for the axial and transverse orientation, while the strain rate sensitivity coefficient is largely orientation independent at 0.151 and 0.178, respectively. Furthermore, the yield stress is decreasing with increasing temperature and water content respectively decreasing loading rate.

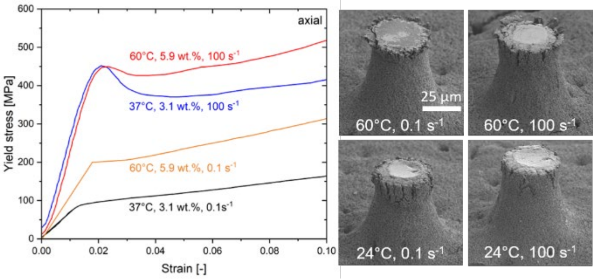

Figure 1: Comparison of micro pillars in axial and transverse orientation compressed at 37°C and 60°C.

Discussion

Applying compressive stresses in axial direction leads to shear stresses, which cause sliding along the interface between the mineral crystals within the extrafibrillar matrix. This ultimately leads to kinking of the fibril bundles, followed by cracking in longitudinal direction. If the fibrils are perpendicular orientated to the loading direction (transverse direction), shear deformation becomes more easily since the deformation can solely takes place within the soft matrix. The small activation volumes indicate a break in the local charge interaction. A highlight of this study is that the effects of temperature and water content on the yield strength could be analyzed separately. In average, a decrease of 7.7 MPa/wt.% in axial and 3.7 MPa/wt.% in transverse direction was found, whereas a minor temperature related decrease of 1.2-1.3 MPa/K was observed. This is in line with earlier studies reporting that deformation most likely takes place in the extrafibrillar matrix [3] and that bounded water has a strong impact on the stress transfer within the matrix and thus on the bone strength.

References

1. N. Reznikov et al., Acta Biomater. 10 (2014) 3815–3826.
2. T.T. Pham et al., T. Theor. Chem. Acc. 134 (2015) 59.
3. H.S. Gupta et al. J. R. Soc. Interface. 4 (2006) 277–282.

Acknowledgements

The authors would like to thank D. Carasi and P. Schweizer for assistance with statistical analysis and modeling.

FRICTIONAL BEHAVIOUR OF CARTILAGE AGAINST POLYCARBONATE URETHANE AND ZIRCONIA – A PIN-ON-DISC IN VITRO STUDY

Roger von Mentlen* (1), Daniel Baumgartner (1)
1. *IMES Institute of Mechanical Systems, Zurich University of Applied Sciences, Switzerland*
**vmro@zhaw.ch*

Introduction

Approximately 5% of the human population and 80% of people older than 65 years suffer from shoulder osteoarthritis (OA) [1]. In cases of OA, one of the two articular surfaces is typically more affected than the other. A hemiprosthesis may preserve the contralateral healthy side, especially in the shoulder. Nevertheless, the articulation characteristics of promising materials such as Polycarbonate-Urethane (PCU) have not been well studied compared to native cartilage. In previous studies PCU showed a threefold lower coefficient of friction against cartilage compared to traditional orthopaedic materials indicating that PCU might be a promising coating for hemiprostheses [2].
The aim of this pilot study is to characterise the coefficient of friction of native cartilage under physiological conditions against Zirconia Toughened Alumina (ZTA) and PCU over time.

Material and Methods

Pin-on-disc tests were conducted to characterize the frictional behaviour of bovine knee cartilage pins against ZTA and PCU. These tests were performed using a compact modular rheometer (Anton Paar, Austria) equipped with a tribology measuring cell (see Figure 1). The tests were carried out under physiological load (0.63 MPa) in Ringer's solution at 37 °C applying test velocities of 15 mm/s and 30 mm/s. Each pairing and test speed was tested with two runs lasting 600 s each, separated by a recovery periof of 300 s between the runs.

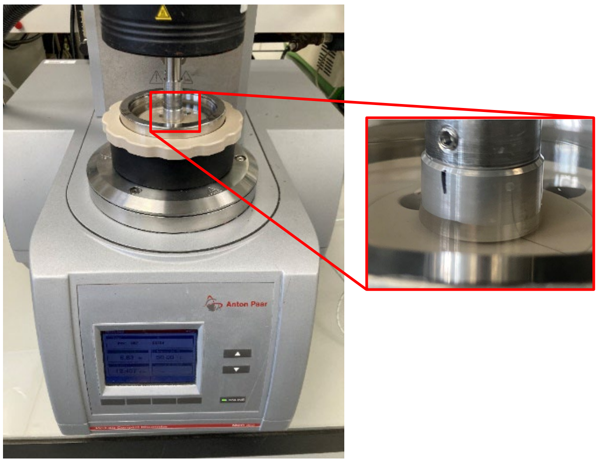

Figure 1: Rheometer with pin-on-disc test setup in Ringer's solution at 37 °C.

Results

Reproducible friction curves of cartilage vs. ZTA and PCU were recorded over time (see Figure 2). The mean coefficients of friction μ(t) of cartilage vs. ZTA is 0.04 to 0.30 and of cartilage vs. PCU is 0.04 to 0.32 (see Figure 3). The friction properties are time dependent.

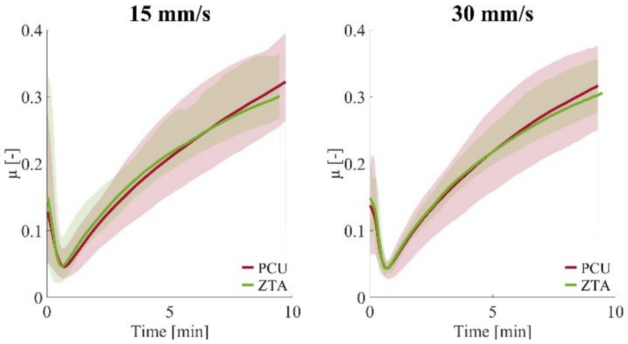

Figure 2: Coefficients of friction μ(t) for cartilage vs. ZTA and PCU at different speeds: 15 mm/s (left) and 30 mm/s (right).

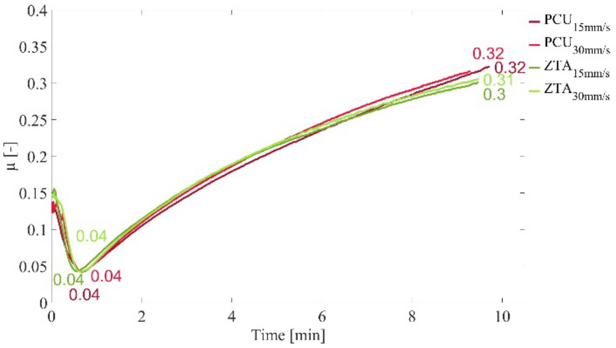

Figure 3: Mean coefficients of friction μ(t).

Discussion

The time-dependent coefficients of friction μ(t) of cartilage against ZTA and PCU show comparable values. During the contact phase, the coefficient of friction increases slightly, decreases while the lubricating film builds up and increases again over the testing period. Further tests are necessary to analyse the long-term behavior of the coefficients of friction, because the plateau has not been reached after 10 min.

References

1. Shi et al, Annals of Biomedical Engineering, 132-146, 2011
2. Sague et al, Combined Meeting of Orthopedic Research, Venice, 2013

A CONTINUUM MECHANICS BASED QUANTIFICATION OF MICROSCALE KINEMATICS OF NANOFIBROUS MEMBRANES

Joël Zimmerli* (1), Jonas Hofmann (1), Barbara Röhrnbauer (1)

1. IMES School of Engineering, ZHAW Zurich University of Applied Sciences, Switzerland
**Corresponding author: zimmejoe@students.zhaw.ch*

Introduction

There is an urgent need for new implant materials for soft tissue and, in particular, pelvic organ prolapse repair [1]. Recent trends are moving toward nanostructured materials, e.g. derived by electrospinning [2]. While there has been research on the clinical, biological and chemical biocompatibility of these new materials, a detailed evaluation of their mechanical biocompatibility is still missing [2]. This study proposes a novel continuum mechanics-based procedure to quantify the inherently inhomogeneous microscale kinematics at the surface of electrospun networks (ESNs). Developed from a numerical model, this method can be directly transferred to experimental observations using SEM-DIC (scanning electron microscopy with digital image correlation). By addressing the cellular length scale, this study shall serve future quantitative mechanobiology investigations.

Material and Methods

A numerical discrete fiber model inspired by the work of Zündel et al. [3] was used to simulate the inhomogeneous deformation patterns of ESNs (Figure 1). The FEM model was used to determine the actual representative volume element (RVE) and representative area element (RAE) sizes. The size of the RAE allows for the definition of a minimum image section that guarantees a representative image of the surface deformations. To this end, a kinematic fingerprint was introduced, which is constituted by the distributions of the relative frequencies of the local Green-Lagrange strains, local deformation types (uniaxial, shear and equibiaxial) and local rotations (Figure 1C, 2). These local kinematic quantities are calculated by subdividing the RAE into small (5–10 um) facets and by homogenizing local fiber deformations over the facet areas. Lastly, deformation tensors from classical continuum mechanics are used, assuming local affine deformations. The standard deviation and mean of the distributions of the local kinematic quantities provide a quantitative fingerprint of the ESN.

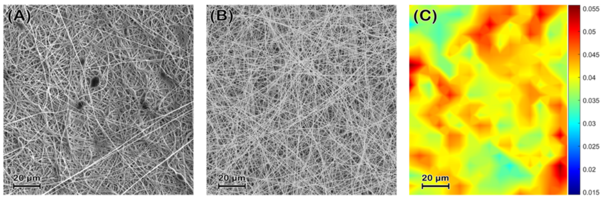

Figure 1: (A) SEM image of an ESN. (B) Visualization of the discrete fiber model. (C) Local distribution of the axial Green-Lagrange strain in uniaxial stress loading conditions.

Results

The fingerprint displays a clear characteristic of the ESNs and their non-affine deformations (Figure 2). The results obtained from the FEM model determined a RVE size of $29 \cdot 10^3$ µm^3 and a RAE size of 160 × 160 µm^2 (depth: 6 µm). The size of the facets turned out to be another crucial parameter. In this study, the minimum facet size was identified to be 5 × 5 µm. It is hypothesized that below this threshold, the assumption of locally affine deformations is no longer valid. This is in accordance with our SEM-DIC investigations.

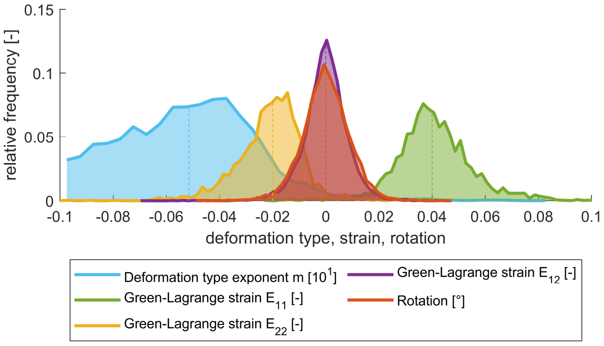

Figure 2: A typical fingerprint of an ESN, showing the distribution of each kinematic quantity. The dashed lines indicate the global affine values.

Discussion

This study presents a methodology for quantifying inhomogeneous deformations in ESNs. The numerical model can be directly applied to develop and validate experimental methods using SEM-DIC. It enables a comprehensive understanding of the deformation behavior at the length scales, which are relevant for biological tissue components. Thus, this study provides a tool for future research in mechanobiology.

References

1. Mancuso et al., J Biomed Mater Res, 108:771-789, 2020.
2. Roman et al., Curr Opin Urol, 29:407–413, 2019.
3. Zündel et al., Soft Matter, 13:6407–6421, 2017.

Acknowledgements

This research was funded in whole by the Swiss National Science Foundation (SNSF). The authors would like to thank the SNSF for the financial support. [PT00P2_206354 / 1]

IMPACT OF INCOMPATIBLE PARTS ON IMPLANT-TO-COVER LEAKAGE

Fabio Bernardoni* (1), Markus Geisendorf (1), Stephanie Ruch (2), Jonas Fabech (2), Chandur Wadhwani (3)

1. Nobel Biocare Services AG, Switzerland; 2. Zürcher Hochschule für Angewandte Wissenschaften (ZHAW), Switzerland; 3. University of Washington, Seattle, WA, United States
*Corresponding author: fabio.bernardoni@envistaco.com

Introduction

A proper fit of prosthetic components on the dental implant is essential in minimizing leakage of contaminants and bacteria, which could compromise the healing and sustained health of peri-implant tissues. A study that compared the performance of anodized vs. sandblasted implant surfaces in an acute dehiscence type defect animal model [1] provides an example of a poor fit of a cover screw on an implant, which impacted bone levels. This investigation aims to specifically compare the tightness of the fit of the implant-to-cover screw connection with two different cover screws, one provided by the original implant manufacturer, and the other non-original screw.

Material and Methods

Test groups consisted of the variable thread tapered implant (NA; NobelActive TiUltra NP Ø 3.5×8.5 mm, Nobel Biocare AB, Göteborg, Sweden) in combination with one of two cover screws: Group G1 with the original Cover Screw NP (Nobel Biocare AB), group G2 with a non-original screw (RB Closure Cap Ø 3.5 mm; H 0.4 mm, Straumann, Basel, Switzerland) which due to incompatibility of components was aligned to the center (best fit) of the implant, and group G3 the same non-original screw placed off-axis [1]. Implants were embedded in an aluminum cylinder and connected to a vacuum pump (adapted ISO14801 setup; Fig. 1). A vacuum was generated, and the pressure change in the implant cavity was monitored at its intended preload in an unloaded condition over a period of 60 seconds (static gas leakage). In the second step, the vacuum was established again within the implant cavity and the pressure change was monitored under loading conditions (dynamic gas leakage), which applies compressive and shear forces over the same period as for the static setup.

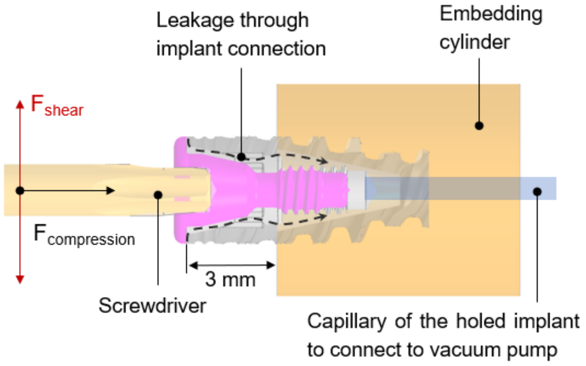

Figure 1: Adapted ISO1489 setup. $F_{compression}$ *was 50 N (constant).* F_{shear} *started at ±14.4 N and increased or decreased by 14.4 N per load cycle. Total 10 cycles.*

Results

Under static conditions, the original screw (G1) provided a tight connection for all 14 specimens, while the tightness with a non-original screw was unreliable (G2: high leakage at 1/15 specimens) or absent (G3: high leakage for all 14 specimens). Under dynamic conditions, G1 supported a significantly tighter connection than the non-original screw from G2 (Fig. 2). Due to the high leakage of G3 at static conditions, this group was not evaluated at dynamic conditions.

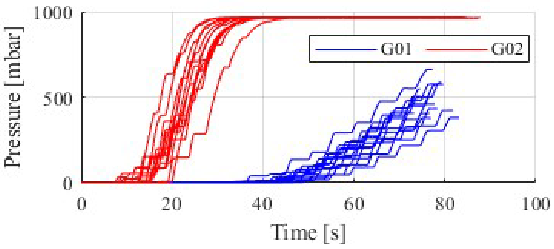

Figure 2: Leakage under dynamic conditions. Note the high leakage with the non-original screw despite the centred alignment (G2, in red) in contrast to the seal provided by the original screw (G1, in blue).

Discussion

The fit of the cover screw can significantly affect the tightness of the screw-implant connection. The original cover screws reliably provided a tight seal under both static and dynamic conditions. By contrast, the non-original screw, even when aligned, was unreliable to provide a seal at static conditions and showed significantly higher leakage at dynamic conditions. When the non-original cover screw was misaligned, similarly to the misalignment shown in a previous study [1], it demonstrated high leakage already at static conditions. These results underscore the importance of the proper prosthetic fit, such as one achieved using original components developed and tested as a system for adequate performance.

References

1. Shahdad, Shakeel et al., Clin Oral Implants Res, 2022.

Acknowledgments

This study was supported by Nobel Biocare grant 2023-1773.

DESIGNING DIRECTION-DEPENDENT FLOW RESISTANCE FOR APPLICATION IN ARTHROPLASTY

Mahdieh Mosayebi* (1), Stephen J. Ferguson (1), Benedikt Helgason (1), Dominik Obrist (2)

1. Institute for Biomechanics, ETH Zurich, Switzerland; 2. 2ARTORG Center for Biomedical Engineering Research, University of Bern, Switzerland

*Corresponding author: mahdieh.mosayebi@hest.ethz.ch

Introduction

Joints can deteriorate due to aging, disease, or trauma, significantly impairing patients' quality of life. Total joint replacements are effective medical solutions that restore joint function and alleviate pain. Recently, there has been a significant rise in arthroplasty demand among both young and elderly patients. However, the typical 15-20 year lifespan of these implants may not meet the needs of younger patients requiring longer-lasting and more durable solutions. Wear and debris are the primary causes of joint implant failure, mitigated by proper lubrication, which enhances longevity and reduces revision surgeries [1]. Natural articulating joints self-lubricate under load, attributed to the poroelastic properties of cartilage and the self-pressurization of interstitial fluid [2]. Despite the critical role of lubrication in reducing friction and wear, self-lubricating prostheses remain unexplored. This study aims to design a novel self-lubricating prosthesis emulating the natural lubrication mechanisms of human joints. As an initial step, various flow obstruction configurations within a 2D rectangular channel were developed to create direction-dependent flow resistance. This design could regulate the net direction and rate of fluid exudation from a mechanical self-pressurizing bearing during cyclic loading.

Material and Methods

To create direction-dependent, nonlinear flow properties, channels with Tesla valve geometries were initially developed [3]. However, Tesla valves, effective in flows dominated by inertia, do not exhibit the same direction dependence at the low physiological synovial fluid velocities generated by joint loading, which are in the millimeters per second range. Inspired by these valves, a design without moving parts was developed using COMSOL Multiphysics 6.2 to create nonlinear resistance to fluid flow through the channel, with fixed semicircular obstacles positioned alongside the channel outlet (Fig.1). Dirichlet Boundary Conditions were applied to assess the nonlinearity and asymmetry of a steady-state flow. Inlet velocities ranged from -50 mm/s to 50 mm/s in 10 mm/s increments at the reservoir's top edge. The outlet pressure at both ends of the lubrication film channel was set to 0 MPa, and the inlet pressure was subsequently calculated.

Results and Discussion

For a constant inlet velocity, a higher inlet pressure indicates a greater flow resistance. The direction-dependent flow resistance was characterized by evaluating the variations in fluid flow behavior when exuding to the lubrication film compared to returning to the reservoir (Fig. 1). Modifications like adding throats, extending the intermediate shell, incorporating a porous layer, adding two more intermediate shells, and reducing distances between flow obstructions independently increased channel resistance and reduced asymmetry (Fig. 2). Conversely, increasing the number of obstacles with a constant gap size reduced resistance but greater asymmetry. This study introduces unique geometric designs that offer distinct resistances to bidirectional flows through a channel of relevant size for joint prostheses, even at small velocity magnitudes, addressing a Tesla valve limitation. These designs have potential in biomedical applications such as prosthesis lubrication and filtration systems.

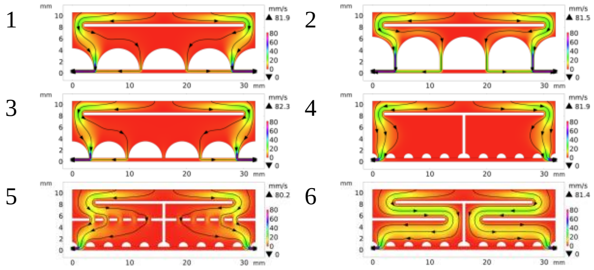

Figure 1: Velocity field of various flow obstruction designs at inlet velocity 2 mm/s. The black lines represent the velocity streamlines.

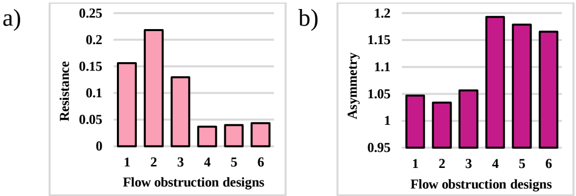

Figure 2: a) The resistance and b) the asymmetry at the velocity 2 mm/s for the six designs depicted in Figure 1.

References

1. L. Gao et al, Lubricants, 10(10):238, 2022.
2. C. McCutchen et al, Nature, 184(4695):1284-5, 1959.
3. P. Cheng et al, Case Stud Therm Eng, 49:103391, 2023.

Acknowledgements

The BioTrib ETN project has received funding from the European Union’s Horizon 2020 research and innovation programme under grant agreement No. 956004.

IN VITRO SIMULATION OF INJECTION FORCES IN SYRINGES: ACCOUNTING FOR FLUID AND NEEDLE PROPERTIES AND BACK PRESSURE

Lucien Python (1), Jonas Fabech* (1), Lea Dal Fabbro (1), Paolo Ravaynia (2), Ainara Irastorza (2)

1. Zürcher Hochschule für Angewandte Wissenschaften (ZHAW), 8401 Winterthur, Switzerland
*2. SHL Medical AG, 6300 Zug, Switzerland *corresponding autor: jonas.fabech@zhaw.ch*

Introduction

Pre-filled syringes are key elements of autoinjectors. Having a good predictability of the force required to expel the medicament from syringes can help accelerate the tailor-made design process of autoinjectors to specific drug doses. This study aims to develop an in vitro model to measure accurately and reproducibly injection forces by varying needles, viscosities, injection speeds, and back pressures. Where back pressure is the resistance in the tissue that builds up during an injection. The experimentally measured values will be compared to a mathematical model.

Material and Methods

The back pressure in the in vitro chamber (Figure 1) ranged from 0 to 1 bar, slightly exceeding Thomson et al.'s range [1]. A 5mL syringe (Hamilton, 1005 TLL) with 23, 25 and 27G needles (25 mm length) was reused during tests, and cleaned with water between uses. Demineralized water (1cp) and glycerol mixtures (10, 20 and 30 cp) were injected with two different flow rates (0.1 and 0.25 mL/s) into the pressure chamber at 20 ±2 °C. The injection force was measured by applying constant displacement to the plunger using a static test machine. Each test case was repeated 3 times, unless aborted if a maximum limit of 100N was reached.

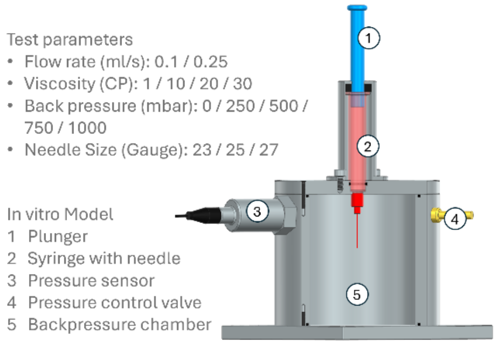

Figure 1 In vitro model for measuring injection force

The mathematical calculation of the injection force (Equation 1) combines Bernoulli and Poiseuille's Law. The pressure loss inside the syringe was neglected due to its low impact [1].

$$F = \pi R^2 \left[\cdot \frac{8\eta l}{\pi r^4} Q + \frac{1.01\rho}{\pi^2 r^4} Q^2 + P_0 + \frac{1}{2} \rho \left(\frac{Q}{\pi r^2} \right)^2 \right]$$

Equation 1: Injection force (F in N) equation based on Bernoulli and Poiseuille's Law, where R and r are the inner radius of syringe and needle (m), l (m) the length of the needle, η is the dynamic viscosity of the fluid (Pa·s), Q the flow rate (m^3/s), Po is the back pressure (Pa) and ρ density (kg/m^3)

Results

Figure 2 compares calculated and experimentally measured injection forces for a 25G needle, showing similar trends as for 23G and 27G needles.

For water, the injection forces were lower than those for glycerol mixtures, with minor deviations between theoretical and experimental results regardless of flow rate and/or back pressure. For glycerol mixtures, the calculated injection force was overestimated. The maximum observed relative error was 42% (23G needle, 0.1 ml/s, 30 cp at 0bar).

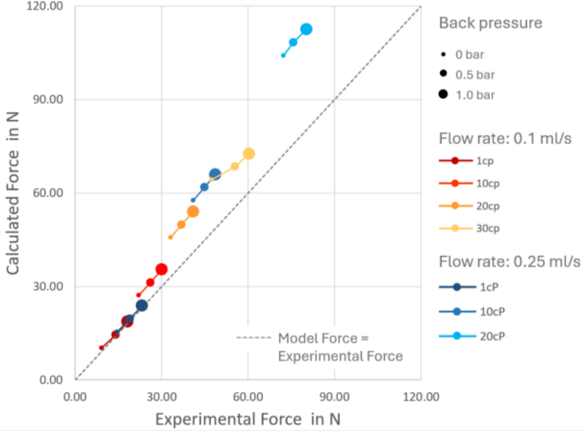

Figure 2 Calculated vs Experimental Force for 25G Needles (30 cp at 0.25ml/s exceeded test limits of 100N)

Discussion

Experimental results show that an increase of flow rate, viscosity, and/or back pressure results in an increase of injection force for all cases.

While the mathematical calculations seem to give an appropriate estimation of the injection force for water, it lacks precision in predicting glycerol mixtures.

Further studies using this in vitro model to mimic back pressure are necessary to refine and verify mathematical calculations. This approach can enhance predictive tools for a wide range of solutions. Additionally, it will help to better understand the factors driving the observed deviations, such as Newtonian and non-Newtonian behaviors.

References

1. Thomson et al., PLoS One. 2014 Aug 14; 9(8): e104054. doi:10.1371/journal.pone.0104054.

Acknowledgements

This project was a not-funded student collaboration between ZHAW and SHL Medical AG.

BEADED ELECTROSURGICAL DISSECTORS: TISSUE & THERMAL ASSESSMENTS

Taiyo C. Weber* (1), Kosei P. Weber (2), Paul J. Weber, MD (3)
1. University of Otago Medical School, New Zealand; 2. Lycee College, Sion, Switzerland; 3. VS, Switzerland
*Corresponding author: TCWeber@ExcelsiorBioVentures.com

Introduction

Electrosurgery is used in ~80% of surgical procedures worldwide.[1] FDA-cleared, patented, beaded dissectors provide simultaneous blunt & sharp dissection with coagulation at speeds multiples that of traditional & current surgical techniques.[2,3,4] Sixteen 100 sqcm dense live porcine tissue plane dissections were performed in 0.8-3 minutes with minimal bleeding. The basic science and potential clinical applications are supported by *ex vivo* and 90-day *in vivo* porcine studies with thermal change quantification by thermocouple, FLIR® thermography and histopathologic measurements. Additionally, *in vivo* studies were assessed photographically, videographically, and ultrasonographically.

Material and Methods

Ex vivo, non-tumesced, porcine models were subject to 1-2cm/sec, single-stroke passage of 20, 30 & 50 Watts assessed by multi-channel thermocouple with matching H&E histopathology. Two *in vivo,* locally tumesced (local anesthesia wetting), porcine subjects experienced eight 10x10cm abdominal, 1-10 cm/sec, dissections (~50% abdominal surface area) at similar wattages and evaluated by university-based veterinarians also assessing histopathology (H&E, collagen, elastin stains) as well as standard and Doppler ultrasounds.

Results

Ex vivo models displayed an average thermal rise of 5°C at 50W; histopathology revealed an average maximal thermal depth effect of 0.09mm (2-bead) and 0.16mm (3-bead). Intraoperatively and postoperatively *in vivo* models experienced minimal bleeding or lipolytic efflux. *In vivo* models histopathologically displayed collagenization and uniformity of dissection planes, as well as occasional resolved small seromas. *In vivo* subjects were eating and walking freely an hour following large, 50% size, complete abdominal dissections. 90-day photographic and clinical assessment demonstrated normal healing parameters in live porcine large abdominal dissections while tissue histopathology and standard ultrasound also confirmed normal healing parameters; Doppler ultrasound demonstrated normal blood flow.

Discussion

Live study bleeding was minimal. 90-day healing was normal. *In vivo* and *ex-vivo* models demonstrated thermal values significantly below those known to clinically damage subcutaneous adipose tissue or skin.

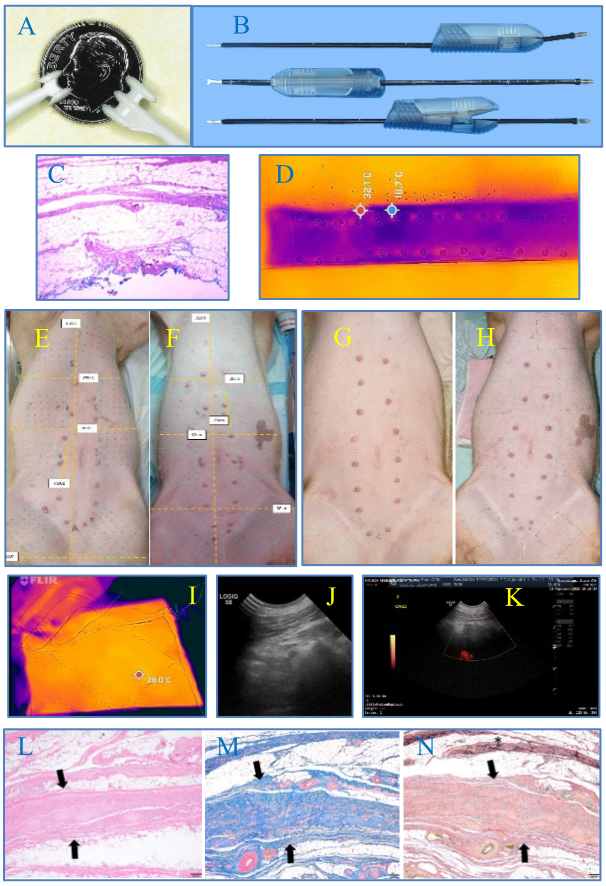

Figures. (A) 2&3-BEED models on 18mm U.S. dime. (B) Ceramic tips on 40cm shafts with adjustable handle. (C) Ex vivo H&E stained histology. (D) FLIR ex vivo image. Top views: (E,F) pre-op & (G,H) 90-days post-op. (I) FLIR in vivo intraoperative. 90-day post-op: (J) standard ultrasound; (K) Doppler u/s; Histopathology: (L) H&E, (M) trichrome-collagen, (N) Van Gieson-elastin.

Conclusion

In vivo and *ex-vivo* studies demonstrated thermal values and clinical support for the safety and efficacy of beaded dissectors in dense porcine subcutaneous adipose tissue models as the devices were operated at speeds many times greater than traditional and current instrument dissections.

References

1. Meeuwsen et al. J. Electrosurgery, 28:247-235, 2019.
2. Weber et al. Aesthetic Surgery J(OF). Minimally Invasive Beaded Electrosurgical Dissectors. Accepted April 2024; expected publication July 2024.
3. FDA clearance 510(k), K233002, 20 Mar 2024.
4. US Patents: us10,603,101; us10,893,899; us10,952,786; us11,510,730; us11,771,489; us11,890,048. EURO Patents: ep3,432,818; ep3,833,288. Plus 55 other country patents issued, 58 more currently pending.
5. Twenty-five further peer-reviewed journal published references (available upon request).

COMPLEMENTARY INTEGRATION OF AFM AND MICROPIPETTE FOR SINGLE-CELL 3D MANIPULATIONS AND NANOMECHANICAL MEASUREMENTS

Yaqi Feng (123), Mi Li* (12)

1. State Key Laboratory of Robotics, Shenyang Institute of Automation, Chinese Academy of Sciences, Shenyang 110016, China; 2. University of Chinese Academy of Sciences, Beijing 100049, China; 3. Laboratory of Biosensors and Bioelectronics, Institute for Biomedical Engineering, ETH Zürich, 8092 Zürich, Switzerland

Introduction

In this work, we present the complementary integration of AFM and micropipette micromanipulation, which allows precise 3D manipulations and nanomechanical measurements of single living cells. The experiments on living animal suspended/adherent cells showed the dramatic changes in cell mechanics in different states and revealed the dynamics of single cells grown on micropillar arrays.

Material and Methods

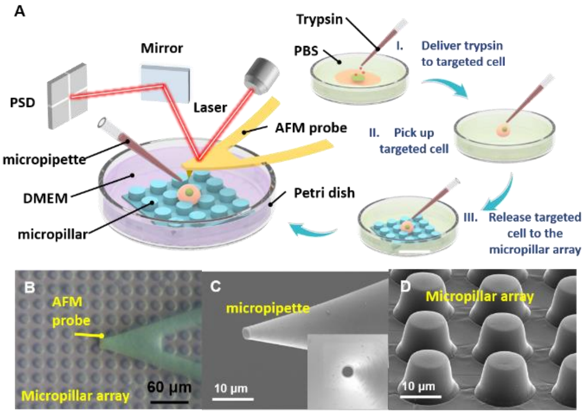

Figure 1: Experimental platform of micropipette-assisted AFM for single-cell 3D manipulations and nanomechanical measurements. (A) Schematic illustration of micropipette-assisted AFM. An example of a living adherent cell is shown. (B) Optical image of moving the AFM probe to detect a single cell which is immobilized in the micropillar array. (C) SEM image of a prepared micropipette. The inset shows the detailed aperture of the micropipette's tip. (D) SEM image of the PDMS micropillar array.

The established micropipette micromanipulation system (*Figure 1*) consists of an inverted optical microscope, a micropipette, a plastic tube, a syringe, a syringe pump, a motorized 3D micro- manipulator and a cell incubator. The syringe was fixed on the syringe pump. The micropipette was attached to the end-effector of the micromanipulator. The plastic tube connects the micropipette to the syringe, which creates a closed system. The micropillar array substrates were fabricated with the use of photolithography and polydimethylsiloxane (PDMS) molding.

Results

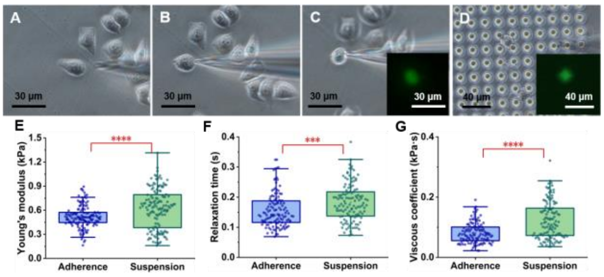

Figure 2: Micropipette-assisted AFM of single living MCF-7 cells. (A–D) Digesting and moving the targeted single MCF-7 cell onto the micropillar array by micropipette-based micromanipulations. (E–G) Statistical results of the Young's modulus (E), relaxation time (F) and viscosity (G) of MCF-7 cells in their adherent states (N = 7) and suspended states (N = 6).

We used the established system to investigate the mechanical changes of single cancer cells in their different states (adherent state and suspended state) during tumor metastasis. During the process of tumor metastasis, cancer cells dramatically change their states.[1,2] Fig. 2(A–D) show the selection and manipulation process of a living MCF-7 cell with the use of a micropipette. Micropillars with a height of 10 μm were used for immobilizing the detached MCF-7 cells. The AFM probe was then controlled to detect the mechanical properties of MCF-7 cells. For control, the mechanical properties of living MCF-7 cells in their adherent states were also measured. The statistical results clearly show that the Young's modulus (Fig. 2E), relaxation time (Fig. 2F) and viscosity (Fig. 2G) of MCF-7 cells in the suspended states were all significantly larger than those in the adherent states.

References

1. L. Keller and K. Pantel, Nat. Rev. Cancer (2019) DOI 10.1038/s41568-019-0180-2. 2
2. D. Wirtz , K. Konstantopoulos and P. C. Searson, Nat. Rev. Cancer (2011) DOI 10.1038/nrc3080.